

# Effects of Anthropogenic Aerosol and Greenhouse Gas Emissions on Northern Hemisphere Monsoon Precipitation: Mechanisms and Uncertainty

PAUL-ARTHUR MONERIE,<sup>a</sup> LAURA J. WILCOX,<sup>a</sup> AND ANDREW G. TURNER<sup>a,b</sup>

<sup>a</sup> National Centre for Atmospheric Science, Reading, United Kingdom

<sup>b</sup> Department of Meteorology, University of Reading, Reading, United Kingdom

(Manuscript received 27 May 2021, in final form 21 December 2021)


**ABSTRACT:** Northern Hemisphere land monsoon (NHLM) precipitation exhibits multidecadal variability, decreasing over the second half of the twentieth century and increasing after the 1980s. We use a novel combination of CMIP6 simulations and several large ensembles to assess the relative roles of drivers of monsoon precipitation trends, analyzing the effects of anthropogenic aerosol (AA), greenhouse gas (GHG) emissions, and natural forcing. We decomposed summer global monsoon precipitation anomalies into dynamic and thermodynamic terms to assess the drivers of precipitation trends. We show that the drying trends are likely to be mainly due to increased AA emissions, which cause shifts of the atmospheric circulation and a decrease in moisture advection. Increases in GHG emissions cause monsoon precipitation to increase due to strengthened moisture advection. The uncertainty in summer monsoon precipitation trends is explored using three initial-condition large ensembles. AA emissions have strong controls on monsoon precipitation trends, exceeding the effects of internal climate variability. However, uncertainties in the effects of external forcings on monsoon precipitation are high for specific periods and monsoon domains, resulting from differences in how models simulate shifts in atmospheric circulation. The effect of AA emissions is uncertain over the northern African monsoon domain due to differences among climate models in simulating the effects of AA emissions on net shortwave radiation over the North Atlantic Ocean.


**KEYWORDS:** Atmosphere; Monsoons; Aerosols; Climate variability; Trends; Tropical variability

## 1. Introduction

Tropical precipitation variability directly impacts billions of people, with the Northern Hemisphere land monsoon (NHLM) regions containing around 60% of the world's population (Wang et al. 2017). The summer monsoons supply most of the annual precipitation to these regions. For instance, the Indian and West African summer monsoons provide about 80% of the total annual rainfall to South Asia and West Africa (Wang et al. 2017). NHLM precipitation decreased between the 1950s to the 1980s and increased afterward (Huang et al. 2019; Zhang and Zhou 2011). Monsoon variability has strong societal effects. The Sahel experienced a severe drought in the 1980s and the early 1990s (Nicholson 2013; Sanogo et al. 2015). According to Zhang and Zhou (2011) and Jin and Wang (2017), Indian precipitation decreased after the second half of the twentieth century and increased in the late 2000s, whereas East Asian precipitation decreased from the 1950s to the 1990s and increased in the early 2000s.

Monsoon precipitation variability has been associated with the effects of internal climate variability and external forcings. Increases in greenhouse gas (GHG) concentrations cause an increase in global mean surface temperature, associated with a strengthening of land–sea thermal contrasts and of the interhemispheric temperature gradient, forcing monsoon circulations to shift northward and favoring the Northern Hemisphere monsoons (Kitoh et al. 2013; Lee and Wang 2014; Moon and Ha 2020; Wang et al. 2020; Chadwick et al. 2019; Park et al. 2015; Cao et al. 2020; D'Agostino et al. 2019). The increase in global mean surface temperature is also associated with an increase in specific humidity in the troposphere (via Clausius–Clapeyron) that contributes to strengthened moisture fluxes and precipitation (thermodynamic effect of climate change) (Kitoh et al. 2013; Monerie et al. 2020b; Chadwick et al. 2016). Although increases in moisture advection act to increase monsoon precipitation, the tropical overturning weakens (Kitoh et al. 2013) due to an increase in gross moist static stability (Bordoni and Schneider 2008; Chou and Chen 2010; Chou et al. 2013; Neelin and Held 1987; Vecchi and Soden 2007; Yu and Neelin 1997), leading to a wind–precipitation paradox (Ueda et al. 2006). The effect of climate change on tropical precipitation is mostly due to thermodynamic changes (Kitoh et al. 2013; Held and Soden 2006; Chadwick et al. 2013), but intermodel uncertainties arise due to uncertainties in projected changes in atmospheric circulation

 Denotes content that is immediately available upon publication as open access.

 Supplemental information related to this paper is available at the Journals Online website: <https://doi.org/10.1175/JCLI-D-21-0412.s1>.

*Corresponding author:* Paul-Arthur Monerie, [p.monerie@reading.ac.uk](mailto:p.monerie@reading.ac.uk)



This article is licensed under a [Creative Commons Attribution 4.0 license](http://creativecommons.org/licenses/by/4.0/) (<http://creativecommons.org/licenses/by/4.0/>).

DOI: 10.1175/JCLI-D-21-0412.1

© 2022 American Meteorological Society.

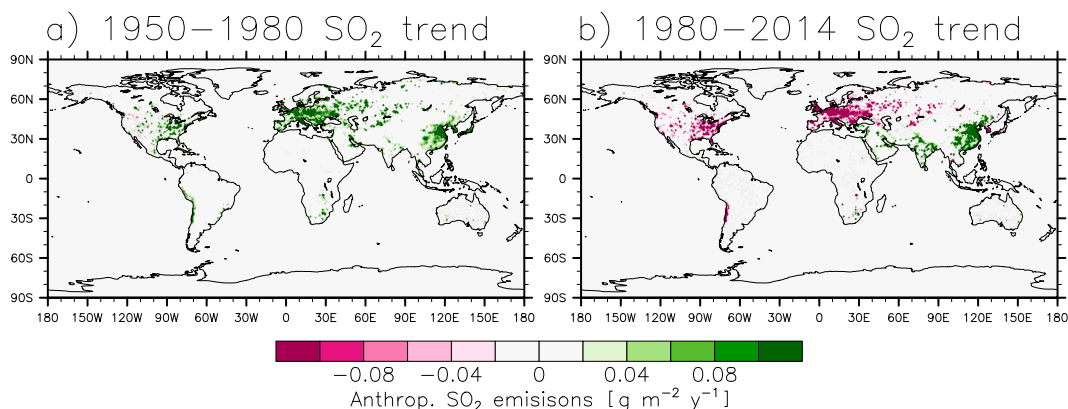


FIG. 1. Trends in sulfur dioxide ( $\text{SO}_2$ ) emissions ( $\text{g m}^{-2} \text{yr}^{-1}$ ) over the periods (a) 1950–80 and (b) 1980–2014. CMIP6 historical forcing is downloaded from input4mips (<https://esgf-node.llnl.gov/search/input4mips/>).

(Kent et al. 2015; Monerie et al. 2020b; Rowell and Chadwick 2018).

Anthropogenic aerosols (AA) can also have strong effects on NHLM precipitation variability (Ackerley et al. 2011; Giannini and Kaplan 2019; Marvel et al. 2020; Bollasina et al. 2011; Wang et al. 2009; Saha and Ghosh 2019; Wang et al. 2019; Westervelt et al. 2020; Ayantika et al. 2021; Polson et al. 2014; Hwang et al. 2013; Herman et al. 2020; Sherman et al. 2021). Emissions of AA and their precursors increased over the United States and western Europe from the preindustrial era to the 1980s and are now decreasing following the introduction of clean air polices. However, Asian AA emissions continue to increase (Wang et al. 2015) (Fig. 1). The overall response to AA is the scattering of shortwave radiation, surface cooling, and a decrease in tropical precipitation (Westervelt et al. 2020; Guo et al. 2013; Persad and Caldeira 2018; Samset et al. 2018; Guo et al. 2016; Polson et al. 2014). AA emissions are spatially heterogeneous, and the change in their primary source regions over time means that the response of each monsoon region has a different aerosol signature. For instance, AA emissions have been associated with a strengthening of the West African monsoon and a weakening of the Indian and East Asian monsoon after the 1980s (Bonfils et al. 2020; Hirasawa et al. 2020; Ackerley et al. 2011; Ayantika et al. 2021; Sherman et al. 2021). Interactions occur between distant regions, with European AA emissions affecting both northern Africa (Ackerley et al. 2011; Dong and Sutton 2015; Dong et al. 2014) and Asia (Dong et al. 2016b), and Asian AA emissions showing large-scale impacts, through changes in warm pool temperature and through Walker-type circulation anomalies (Dong et al. 2014) that also impact the tropical Atlantic Ocean (Undorf et al. 2018). Besides AA and GHG emissions, natural (NAT) forcings could affect low-frequency monsoon precipitation variability, through the solar cycle (van Loon et al. 2004; Meehl et al. 2009) and volcanic eruptions (Zuo et al. 2019). Volcanic activity was shown to have strong impacts on monsoon precipitation, one year following major eruptions (Haywood et al. 2013; Liu et al. 2016; Herman et al. 2020; Jacobson et al. 2020) and depending on the location of the eruption.

In addition to the influence of external forcings, modes of internal climate variability have strong effects on monsoon precipitation variability. The low-frequency variability in NHLM precipitation is associated with changes in sea surface temperatures (SSTs) (Wang et al. 2018). Atlantic multidecadal variability (AMV), Pacific decadal variability (PDV), and Indian Ocean SST variability all have strong effects on NHLM monsoon precipitation (Wang et al. 2018; Giannini et al. 2003; Monerie et al. 2019; Krishnamurthy and Krishnamurthy 2014; Zhang et al. 2018; Huang et al. 2020).

Climate models have large biases, underestimating precipitation means and variability over monsoon domains (Pathak et al. 2019; Monerie et al. 2020b; Wilcox et al. 2020). Biases in simulating the multidecadal variability in monsoon precipitation limit our ability to simulate and predict monsoon precipitation. One of the causes of these biases is the uncertainty in simulating the effects of external forcing on monsoon precipitation variability. In addition, intermodel spread in the response to forcing can result from the diversity in pattern and magnitude of the forcing, which arises as due to differences in model physical processes and climatologies (Wilcox et al. 2015; Shonk et al. 2020).

Documenting and understanding effects of anthropogenic forcings, over the historical record, is an outstanding issue that would help understand climate variability and biases in climate simulations. In this study, we assess the effects of external forcings, including AAs, GHGs, and natural forcings (NAT; i.e., volcanism, solar cycle), on NHLM precipitation. We make use of the new generation of climate models, made available thanks to phase 6 of the Coupled Model Intercomparison Project (CMIP6; Eyring et al. 2016), and use simulations performed for the Detection and Attribution Model Intercomparison Project (DAMIP; Gillett et al. 2016), to assess, separately, the effects of the AA, GHG, and NAT forcings (see section 2). We gather new information by employing a decomposition method that enables analysis of terms that have not so far been assessed for historical monsoon precipitation trends: anomalies associated with dynamic shifts of the circulation and with a weakening of the tropical mean circulation, for instance. The CMIP6 multimodel

TABLE 1. List of models and number of simulations used in the study.

Models	Institutions	No. of ensemble members for each simulation	References
ACCESS-ESM1-5	Australian Community Climate and Earth System Model, Australia	3	Ziehn et al. (2020)
BCC-CSM2-MR	Beijing Climate Center, China	3	Shi et al. (2020)
CanESM5	Canadian Centre for Climate Modeling and Analysis, Canada	30	Swart et al. (2019)
CNRM-CM6-1	Centre National de Recherches Météorologiques, France	10	Voltaire et al. (2019)
FGOALS-G3	Chinese Academy of Sciences, China	3	Li et al. (2020)
HADGEM3-GC31-LL	Met Office Hadley Centre, United Kingdom	3	Kuhlbrodt et al. (2018)
GISS-E2-1-G	Goddard Institute for Space Studies, United States	3	Kelley et al. (2020)
IPSL-CM6A-LR	Institut Pierre Simon Laplace, France	10	Boucher et al. (2020)
MIROC6	Japanese modeling community, Japan	3	Tatebe et al. (2019)
MRI-ESM2-0	Meteorological Research Institute, Japan	3	Yukimoto et al. (2019)

ensemble, together with the availability of initial-condition large ensembles from several modeling groups, provides us the opportunity to assess the role of both externally forced change and internal variability. This study is a first attempt to quantify the model uncertainty that is associated with each of the aforementioned external forcings.

The paper is organized as follows: section 2 describes the simulations and the methodologies used. In section 3, we assess effects of external forcings on NHLM monsoon precipitation, expanding on the mechanisms, decomposing precipitation anomalies. Section 4 shows regional changes in temperature and atmospheric circulation, to explain monsoon precipitation anomalies. Uncertainties in simulating effects of external anthropogenic forcing are assessed in section 5. Section 6 provides conclusions.

## 2. Data and method

### a. Observations

Different observational datasets provide different representations of the real world. We ensure that our results are not tied to only one dataset by using several observational datasets: the Global Precipitation Climatology Centre (GPCC) version 7 (Schneider et al. 2014) dataset, which is available from 1901 to the present on a  $0.5^\circ \times 0.5^\circ$  grid; the Climate Research Unit (CRU; version 4.01) dataset allows an estimation of precipitation at a  $0.5^\circ$  horizontal resolution from 1901 to 2016 (Harris et al. 2014); the Precipitation Reconstruction over Land (PREC/L) dataset is at  $1.0^\circ$  horizontal resolution and is available from 1948 to the present (Chen et al. 2002); and the University of Delaware (UDEL; Willmott et al. 2001) dataset is at  $0.5^\circ$  horizontal resolution from 1901 to 2014. We also used wind and temperature data from the National Centre for Environmental Prediction (NCEP) reanalysis (R-1; Kanamitsu et al. 2002), which is given from 1948 to the present and at  $2.5^\circ$  resolution ( $144 \times 72$ ) with 17 vertical levels.

### b. CMIP6 simulations

We use historical simulations from phase 6 of the Coupled Model Intercomparison Project (CMIP6; Eyring et al. 2016)

to assess model performance and effects of external forcings on NHLM precipitation. These simulations are from ocean–atmosphere coupled general circulation models (AOGCMs), and cover the 1850–2014 period, using historical external forcing (e.g., greenhouse gases, anthropogenic aerosols, solar cycle, volcanic activity) (Eyring et al. 2016). The physical complexity of climate models has increased since CMIP5, with CMIP6 models including more comprehensive representations of aerosol–cloud interactions (Collins et al. 2017). We used three ensemble members of 10 CMIP6 climate models (Table 1). However, the full spread of internal climate variability is unlikely to be sampled by the three members, and so we address this by using single-model initial-condition large ensembles (SMILEs; e.g., Deser et al. 2012). This also incorporates testing the effects of model uncertainty since three SMILEs were available: 30 members of CanESM5, and 10 members each of IPSL-CM6A-LR and CNRM-CM6-1. The combination of the latest CMIP6 multimodel ensemble and this collection of SMILEs provides a unique way of assessing the roles of external and internal forcing on multidecadal monsoon variability.

We assess roles of external forcing with single-forcing simulations from DAMIP (Gillett et al. 2016), whose design enables an assessment of the effects of variations in AA, GHG emissions, and NAT forcings:

- The greenhouse gas–only simulations (hist-GHG) resemble the historical simulations but are instead forced by the changes in well-mixed greenhouse gas only, derived from the historical simulations, and allow assessment of the effects of changes in GHG concentration.
- Historical aerosol–only simulations (hist-AER) resemble the historical simulations but are forced by the changes in anthropogenic aerosol forcing only [black carbon, organic carbon,  $\text{SO}_2$ ,  $\text{SO}_4$ ,  $\text{NO}_x$ ,  $\text{NH}_3$ , CO, non-methane volatile organic compounds (NMVOCs)].
- Natural-only simulations (hist-NAT) resemble the historical simulations but are forced with only solar and volcanic forcings.

We extract the effects of the AA, GHG, and NAT forcings by computing linear trends in the hist-AER, hist-GHG, and

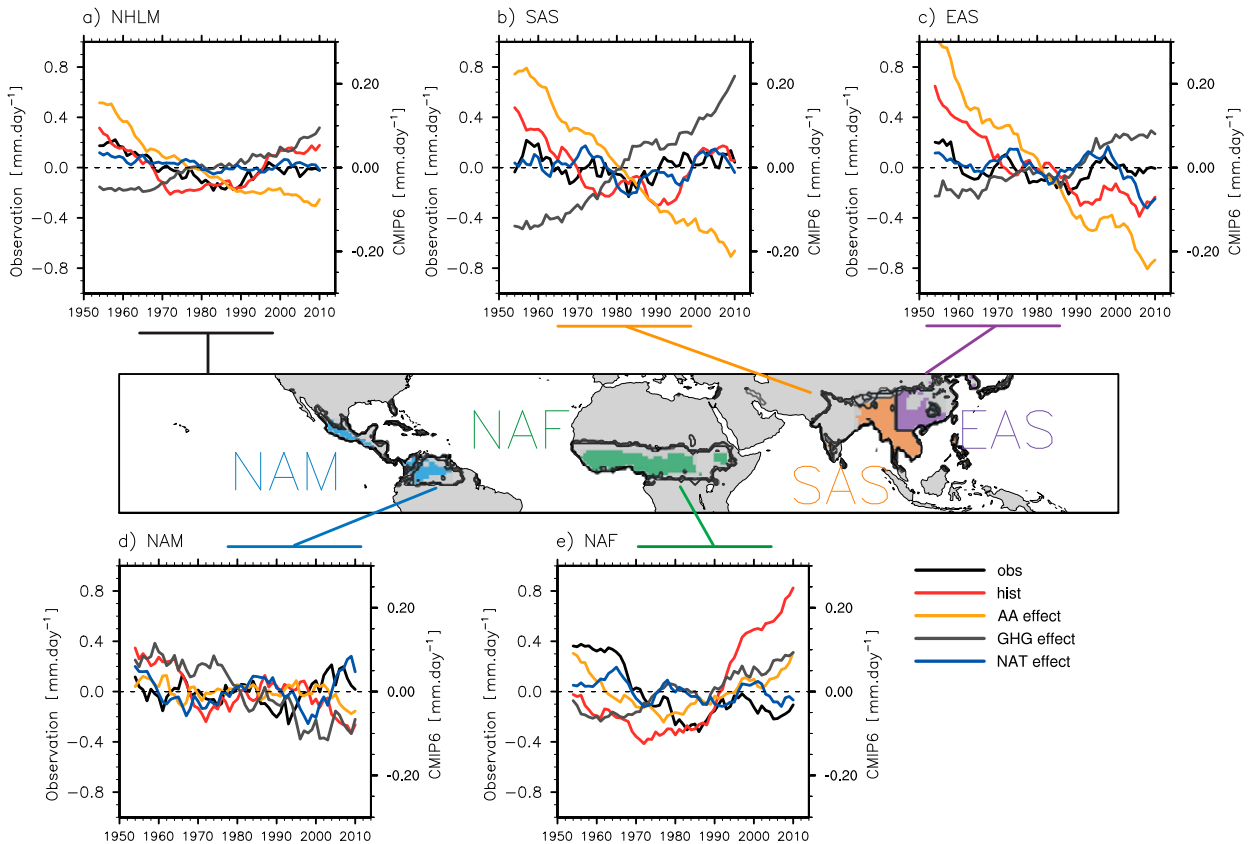


FIG. 2. Observed (gray contours for GPCP, CRU, UDEL, and PRECL) and simulated (grid points are shown in color when at least 80% of the models agree that it is covered by a monsoon) monsoon domains. Area-weighted MJJAS monsoon precipitation anomaly ( $\text{mm day}^{-1}$ ) is given for the (a) NHLM, (b) SAS, (c) EAS, (d) NAM, and (e) NAF monsoon domains for GPCP (black), the ensemble mean of the historical CMIP6 simulations (red), the AA (yellow), GHG (gray), and NAT (blue) effects, given by the ensemble mean of the hist-AER, hist-GHG, and hist-NAT simulations, with the primary and secondary y axis, respectively. Precipitation anomalies are calculated relative to the period 1950–2014. A 9-yr running mean is applied to extract low-frequency monsoon precipitation variability.

hist-NAT simulations over periods chosen to capture the main features of observed decadal variability in NHLM precipitation. We denote these trends as the AA effect, GHG effect, and NAT effect, respectively.

### c. Method

#### 1) MONSOON DOMAINS

Global monsoon domains are defined, for both observations and simulations, following Wang et al. (2011). We select grid points where the annual precipitation range [i.e., the difference between May–September (MJJAS) and November–March (NDJFM)] exceeds  $2.5 \text{ mm day}^{-1}$ . Monsoon domains are displayed in Fig. 2. The NHLM monsoon domain is composed of the NAM (North America), NAF (North Africa), SAS (South Asia), and EAS (East Asia) subdomains (Wang et al. 2011).

Climate models have biases, and the simulation of monsoon precipitation is model-dependent. Therefore, applying a single domain across multiple models will include areas that are not covered by a monsoon in several models, where precipitation variability is significantly lower, and is likely to result in

an artificially suppressed trend. The monsoon domains are thus computed for observations and each model separately. Most models simulate an anomalously low annual precipitation range, especially over India (see Fig. S1 in the online supplemental material) and the monsoon domains are smaller in the models than in observations (Fig. 2a). We used three alternative methods to test the sensitivity of this result to the methodology: using a smaller  $2 \text{ mm day}^{-1}$  absolute threshold, using a relative threshold (based on the observed annual precipitation range) (not shown), and applying the observed monsoon domains to CMIP6 simulations (Fig. S2). The results are qualitatively similar in each case.

#### 2) TRENDS IN PRECIPITATION AND MULTIMODEL MEAN

We perform a multimodel mean (MMM) to show trends in monsoon precipitation associated with the different forcings. The multimodel mean reduces biases and outperforms individual models (Randall et al. 2007), and allows internal climate variability to be filtered out, extracting the effects of individual forcings on monsoon precipitation.



We compare observations to simulations over specific periods, chosen to capture changes in the sign of NHLM precipitation trends (Fig. 2a). We chose the period 1950–80 during which NHLM precipitation decreased, and the period 1980–2014, during which NHLM precipitation increased (Fig. 2a). These periods coincide with changes in trends in European and American AA: the period 1950–80 allows us to define effects of an increase in AA emissions on climate (Fig. 1a), whereas the use of the period 1980–2014 allows assessment of the effects of decreases in European and American AA emissions, while Asian emissions continue to increase (Fig. 1b). GHG emissions have increased from 1950 to the present, but with a rate that has increased since the early 1980s.

Throughout the study, we show time series and trends in summer monsoon precipitation, averaging precipitation over the MJJJ period, to account for the boreal summer.

### 3) DECOMPOSITION OF PRECIPITATION ANOMALIES

We assess mechanisms by which external forcing affects monsoon precipitation by decomposing precipitation anomalies into terms that document both dynamic and thermodynamic changes. We follow Held and Soden (2006), who assumed that precipitation anomalies can be approximated by

$$P = M^* q, \quad (1)$$

where  $P$  is precipitation,  $M^*$  is a proxy for convective mass flux from the boundary layer to the free troposphere, and  $q$  is the near-surface specific humidity. Within this proxy we assume that tropical precipitation is dominated by convection. This was shown to be true within climate models (Chadwick et al. 2013, 2016). From Eq. (1),

$$\Delta P = \Delta(M^* q), \quad (2)$$

with  $\Delta$  indicating anomalies in precipitation, computed relative to the climatology, which we have defined as the 1950–2014 period. Here, a high precipitation rate implies large convective mass flux, when convection is pumping up air with a high specific humidity from the boundary layer.

Precipitation anomalies are then reformulated in terms of a dynamic ( $\Delta P_{\text{dyn}}$ ), a thermodynamic ( $\Delta P_{\text{therm}}$ ), and a cross nonlinear ( $\Delta P_{\text{cross}}$ ) component, following Chadwick et al. (2016):

$$\Delta P = M^* \Delta q + q \Delta M^* + \Delta q \Delta M^*, \quad (3)$$

which we can reformulate as

$$\Delta P = \Delta P_{\text{therm}} + \Delta P_{\text{dyn}} + \Delta P_{\text{cross}}, \quad (4)$$

where  $\Delta P_{\text{therm}}$  is the change in precipitation due to the change in specific humidity, with no change in atmospheric circulation (i.e., the thermodynamic term),  $\Delta P_{\text{dyn}}$  is the change in precipitation that is due to a change in atmospheric circulation, with no change in specific humidity availability (i.e., the dynamic term), and  $\Delta P_{\text{cross}}$  is the change in precipitation due to changes in both specific humidity and atmospheric circulation.

We further decompose  $\Delta P_{\text{dyn}}$  and  $\Delta P_{\text{therm}}$  into two subcomponents. The term  $\Delta P_{\text{dyn}}$  is due to changes relating to a

weakening of the tropical mean circulation ( $\Delta P_{\text{weak}}$ ), and due to anomaly pattern in atmospheric circulation ( $\Delta P_{\text{shift}}$ ), as

$$\Delta P_{\text{weak}} = q \Delta M_{\text{weak}}^* \quad \text{and} \quad (5)$$

$$\Delta P_{\text{shift}} = q \Delta M_{\text{shift}}^*, \quad (6)$$

with

$$\Delta M_{\text{weak}}^* = -\alpha M^*, \quad (7)$$

where

$$\alpha = -\left(\frac{\text{tropical mean } \Delta M^*}{\text{tropical mean } M^*}\right). \quad (8)$$

The tropical mean is computed between 30°S and 30°N. The precipitation anomaly associated with shifts in the circulation is computed as a residual from the weakening of the tropical mean circulation, as

$$\Delta M_{\text{shift}}^* = \Delta M^* - \Delta M_{\text{weak}}^*, \quad (9)$$

Then  $\Delta P_{\text{therm}}$  is decomposed into a sum of terms documenting moisture advection ( $\Delta P_{\text{qadv}}$ ) and a residual ( $\Delta P_{\text{res}}$ ). The advection term is calculated over land, as

$$\Delta P_{\text{qadv}} = M^* \Delta q_{\text{adv}}, \quad (10)$$

with

$$\Delta q_{\text{adv}} = q_{\text{land\_anomaly}} - q_{\text{land}}, \quad (11)$$

with  $q_{\text{land\_anomaly}}$  obtained by scaling  $q_{\text{land}}$  by the zonal mean fractional change in  $q_{\text{ocean}}$  (i.e., the specific humidity over the ocean only) at the same latitude, with no change in the circulation. The residual is calculated as

$$\Delta P_{\text{res}} = M^* \Delta q_{\text{res}}, \quad (12)$$

with

$$\Delta q_{\text{res}} = \Delta q - \Delta q_{\text{adv}}. \quad (13)$$

A warming of the tropical mean sea surface temperature is associated with both a weakening of the tropical mean circulation ( $\Delta P_{\text{weak}}$ ) and with an increase in moisture advection  $\Delta P_{\text{qadv}}$ . Therefore, there is a cancellation of both terms and we then combined them to give  $\Delta P_{\text{weakadv}}$ :

$$\Delta P_{\text{weakadv}} = \Delta P_{\text{qadv}} + \Delta P_{\text{weak}}. \quad (14)$$

The term  $\Delta P_{\text{res}}$  corresponds to the change in precipitation that is due to changes in specific humidity, but with no change in moisture advection;  $\Delta P_{\text{res}}$  is seen as a residual term that is associated with changes in the circulation (Rowell and Chadwick 2018; Chadwick et al. 2016).

The combination of  $\Delta P_{\text{shift}}$  and  $\Delta P_{\text{res}}$  provides the change in precipitation that is associated with dynamic changes (but with no change of the mean tropical circulation) ( $\Delta P_{\text{shiftres}}$ ):

$$\Delta P_{\text{shiftres}} = \Delta P_{\text{shift}} + \Delta P_{\text{res}}. \quad (15)$$

The decomposition is performed using monthly means of precipitation and surface specific humidity prior to computing the seasonal means (i.e., May–September) and area-weighted averages.

#### 4) HIERARCHICAL CLUSTERING

We explore how internal variability can modulate effects of external forcing on monsoon precipitation anomalies by showing similarities between the monsoon precipitation trends produced in each simulation. We assess dissimilarity between spatial patterns in monsoon precipitation trends using an agglomerative hierarchical clustering (AHC) algorithm (Jain et al. 1999). The AHC algorithms create a nested sequence of partitions of the patterns from the dissimilarity matrix. The AHC merges clusters that are closest according to a Euclidean distance, using Ward's method that minimizes the sum of squared differences within all clusters (Ward 1963). The AHC has been used to classify monthly rainfall anomalies (Ullmann et al. 2014) and models (Monerie et al. 2017). The hierarchical clustering is applied using the SciPy linkage Python function. The spatial patterns classified are the MJJAS 1950–80 and 1980–2014 trends in NHLM precipitation, by only considering grid points that are included within the NAM, NAF, SAS, and EAS observed monsoon domains. The analysis is performed on the spatial pattern correlation matrix in precipitation trends, computed from 30 simulations (10 models  $\times$  3 simulations for each model), that is, from a  $30 \times 30$  spatial correlations matrix. We display results on a dendrogram. Short distances between ensemble members indicate a high degree of similarity between simulated spatial trends in monsoon precipitation.

### 3. Trends in monsoon precipitation

#### a. NH monsoon precipitation trends

The observed NHLM precipitation decreases between 1950 and the 1980s, and increases afterward (Fig. 2a), as shown in Zhang and Zhou (2011). Although it underestimates the magnitude of multidecadal precipitation variability, the historical MMM broadly reproduces the timing of observed variability in NHLM monsoon precipitation. This suggests that the observed timing of low-frequency NHLM monsoon precipitation change is partly forced by external drivers prescribed in CMIP6. While changes in anthropogenic aerosols (AA) are associated with a decrease in NHLM monsoon precipitation, changes in greenhouse gases (GHG) are associated with an increase in NH monsoon precipitation (Fig. 2a). Natural external forcings (NAT) are associated with moderate changes in precipitation, showing no effects over the long term. Qualitatively, these results suggest that the simulated 1950–80 drying is mostly attributed to increases in AA emissions, while post-1980s increase in precipitation is attributable to the increases in GHG concentrations (Fig. 2a), as shown

in Giannini and Kaplan (2019), Herman et al. (2020), and Ayantika et al. (2021).

Most of the individual monsoon domains show a similar behavior to the global NHLM domain. The observed SAS, EAS, and NAF precipitation decreases from the 1950s to the 1980s (Figs. 2b,c,e). The observed NAM precipitation increases in the early 1990s, but there are no strong trends in the mid-twentieth century (Fig. 2d). Figure S3 shows that results do not depend on observations.

Simulated SAS precipitation reaches a minimum later than observed (in the 1990s compared to the observed minimum in the 1980s) (Fig. 2b). The models also fail to simulate the post-1990s increase in EAS precipitation (Fig. 2c). The CMIP6 ensemble mean underestimates the drying trend and overestimates the positive trend in NAF precipitation (Fig. 2e). CMIP6 simulations are not able to reproduce the observed variability of NAM precipitation (Fig. 2d). Differences between observed and simulated monsoon precipitation trends can be due to effects of internal climate variability and to model biases.

The decrease in European and North American AA emissions occurs on similar time scales and can contribute to an increase in NAF precipitation (Fig. 2e) (Giannini and Kaplan 2019). The GHG effect is an increase in precipitation at the global scale and over most of the monsoon domains (NAF, EAS, and SAS) but is associated with a decrease in NAM precipitation (Fig. 2d) [consistent with Karmalkar et al. (2011)]. NAT forcings have strong impacts on the precipitation variability, but do not explain long-term trends in precipitation.

#### b. Decomposing trends in NHLM monsoon precipitation (1950–80)

We decompose tropical precipitation anomalies to explain drivers of precipitation trends. A majority of observations show that the negative trend in NHLM precipitation is mostly due to dynamic changes (i.e.,  $\Delta P_{\text{dyn}}$ ) through a shift in the atmospheric circulation (i.e.,  $\Delta P_{\text{shift}}$ ) (Fig. 3a), as also shown in Huang et al. (2019). Thermodynamic changes (i.e.,  $\Delta P_{\text{therm}}$ ) and nonlinear changes (i.e.,  $\Delta P_{\text{cross}}$ ) are negligible (Fig. 3a). There are discrepancies among observations regarding the mechanisms at play, with PRECL showing a stronger role of thermodynamic changes and a weaker role of dynamic changes than the other datasets (Fig. 3a).

In CMIP6 historical simulations, the decrease in NHLM precipitation is mostly due to a shift in the circulation (Fig. 3c;  $\Delta P_{\text{dyn}}$  and  $\Delta P_{\text{shift}}$ ), while thermodynamic terms are of moderate intensity (Fig. 3c;  $\Delta P_{\text{therm}}$  and  $\Delta P_{\text{adv}}$ ). This is consistent with the observations. The AA forcing is associated with a decrease in precipitation over the Northern Hemisphere (Fig. 2a), through a shift of the atmospheric circulation and a decrease in moisture advection (Fig. 3e), consistent with the behavior of CMIP5 models shown by Zhou et al. (2020). There is a slight strengthening of the tropical mean circulation that brings a significant amount of precipitation over land (i.e.,  $\Delta P_{\text{weak}}$ ), but the combination of the decrease in moisture advection and the change of the tropical mean circulation leads to a slight decrease in precipitation (i.e.,  $\Delta P_{\text{weakadv}}$ ).

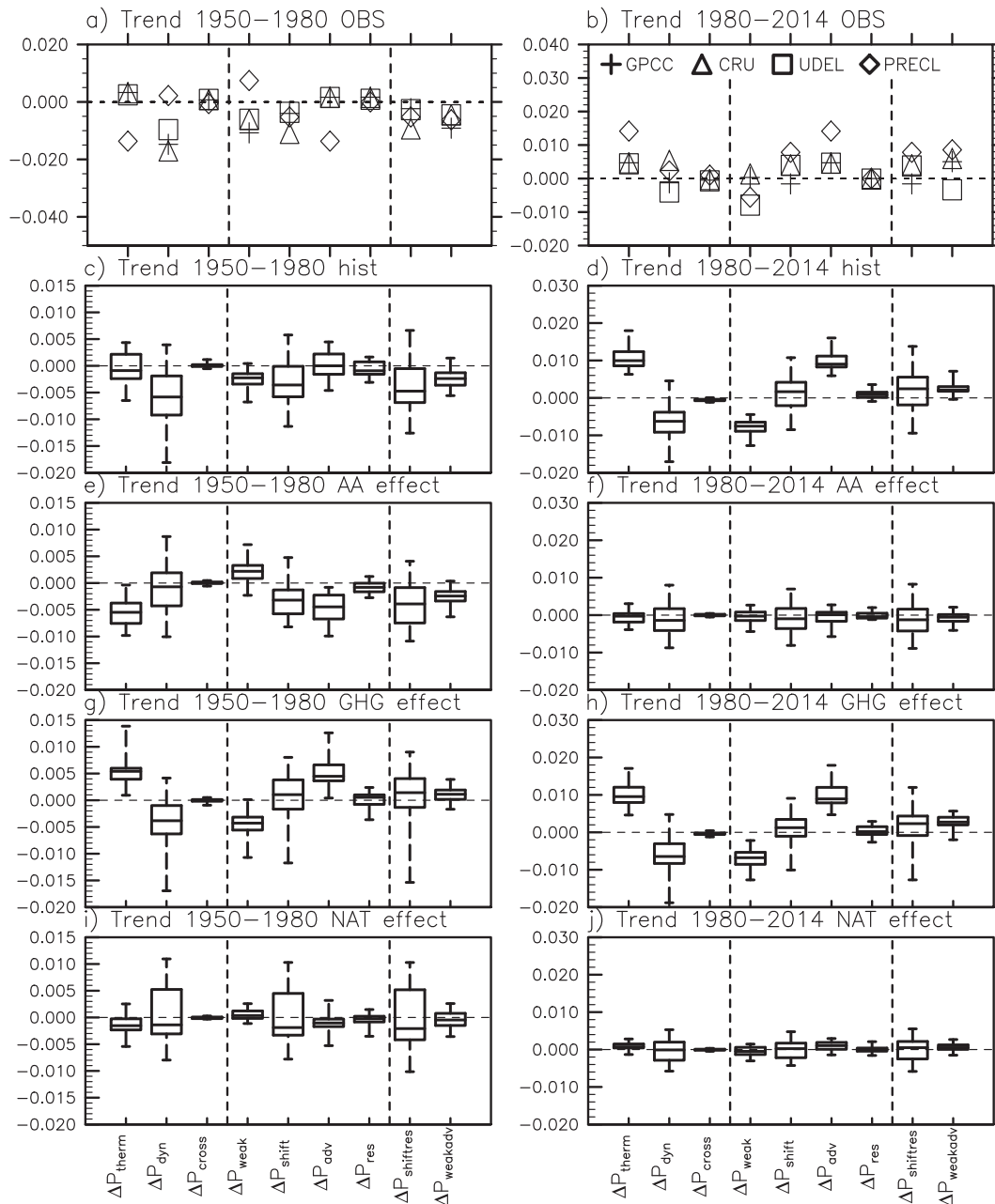


FIG. 3. Trends in NHLM precipitation terms ( $\Delta P_{\text{therm}}$ ,  $\Delta P_{\text{dyn}}$ ,  $\Delta P_{\text{weak}}$ ,  $\Delta P_{\text{shift}}$ ,  $\Delta P_{\text{adv}}$ ,  $\Delta P_{\text{res}}$ ,  $\Delta P_{\text{shiftres}}$ , and  $\Delta P_{\text{weakadv}}$  plotted from left to right in each panel;  $\text{mm day}^{-1} \text{yr}^{-1}$ ) in MJJAS and for (a),(b) observations (GPCC, CRU, UDEL, and PRECL), (c),(d) historical simulations, (e),(f) anthropogenic aerosol only simulations, (g),(h) GHG-only simulations, and (i),(j) natural forcing only simulations. Results are given for the (a),(c),(e),(g),(i) 1950–80 trend and (b),(d),(f),(j) 1980–2014 trend. GPCC, CRU, UDEL, and PRECL are shown with a cross, a triangle, a square, and a diamond, respectively. Box-and-whisker plots are for trends in NHLM precipitation in CMIP6 simulations. The plots show the 25th, 50th, and 75th percentiles (represented by the boxes) and the maximum and minimum values (shown by the extent of the whiskers).

Changes in GHG concentrations are associated with an increase in NHLM monsoon precipitation (Fig. 2a). It allows for increasing moisture content in the air (i.e., Clausius-Clapeyron) and therefore strengthening advection (i.e.,  $\Delta P_{\text{adv}}$ ) (Fig. 3g). Meanwhile, the warming of the ocean is associated

with a weakening of the atmospheric circulation (i.e.,  $\Delta P_{\text{weak}}$ ) (Fig. 3g). These changes are significantly negatively correlated and oppose each other (i.e.,  $\Delta P_{\text{weakadv}}$  is rather low), obscuring the positive effect of the increase in moisture advection on precipitation. Opposing effects of dynamic and thermodynamic

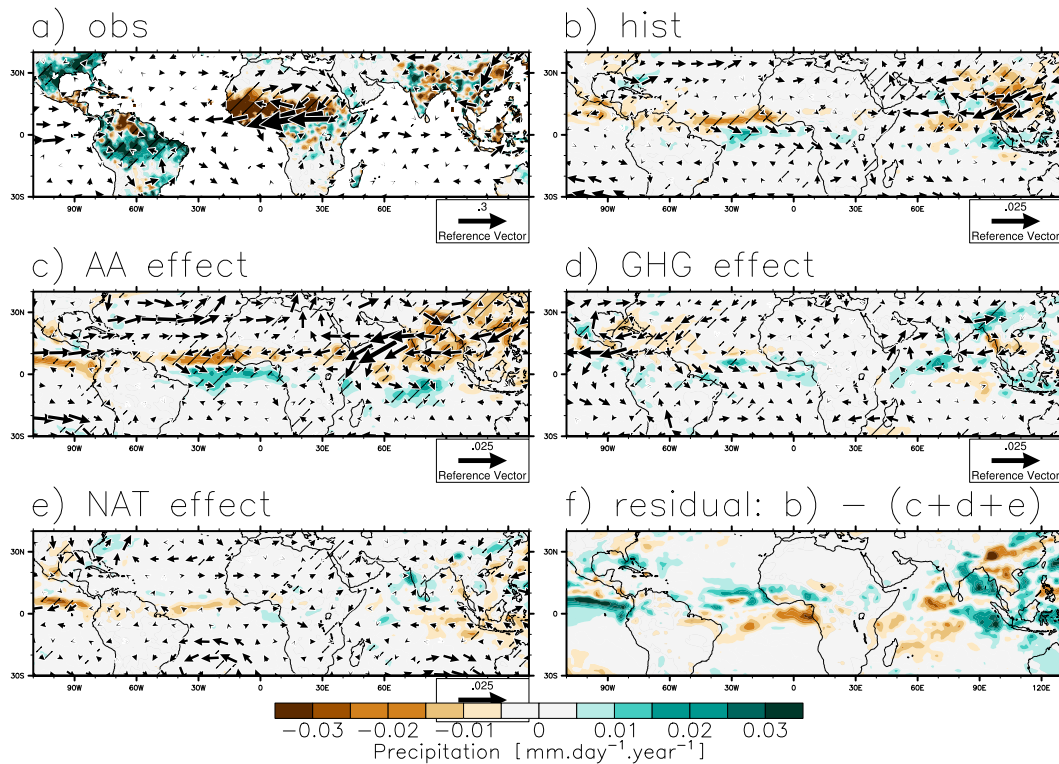


FIG. 4. Trends in precipitation ( $\text{mm day}^{-1} \text{yr}^{-1}$ ; colors) and 850-hPa wind ( $\text{m s}^{-1} \text{yr}^{-1}$ ; arrows) from 1950 to 1980 in MJJAS. Trends are shown for each grid point and (a) for the observation/reanalysis (GPCC and NCEP), for the ensemble mean of the (b) historical, (c) hist-AER, (d) hist-GHG, and (e) hist-NAT, and (f) for the residual between the historical simulations and the sum of all forcings. Stippling indicates that precipitation trends are significant at the 95% confidence level according to Student's  $t$  test.

changes are consistent with previous studies (Kitoh et al. 2013; D'Agostino et al. 2019, 2020; Monerie et al. 2020a; Zhou et al. 2020). Natural forcings are not associated with substantial changes in NHLM precipitation (Fig. 2a) and precipitation components show only small trends (Fig. 3i).

### c. Decomposing trends in NHLM monsoon precipitation (1980–2014)

In observations, the 1980–2014 increase in NHLM precipitation is associated with both an increase in specific humidity (i.e.,  $\Delta P_{\text{therm}}$ ) and changes of the atmospheric circulation (i.e.,  $\Delta P_{\text{shiftrcs}}$ ) (Fig. 3b). Increases in moisture advection are partially obscured by the large-scale weakening of the tropical mean circulation, leading to positive precipitation anomalies due to  $\Delta P_{\text{weakadv}}$ . Shifts in atmospheric circulation (i.e.,  $\Delta P_{\text{shiftrcs}}$ ) allow NHLM precipitation to increase.

In CMIP6 historical simulations, the positive precipitation trend is mostly due to thermodynamic changes (moisture advection), but which are partially counteracted by a weakening of the mean tropical circulation (Fig. 3d). Trends in NHLM precipitation components are similar in historical (Fig. 3d) and hist-GHG (Fig. 3h) simulations, showing a strong control of the GHG forcing on NHLM precipitation after 1980. The AA effect on the 1980–2014 NHLM

precipitation trend is moderate (Fig. 3f). However, strong effects of AA emissions are shown on regional scales (Fig. S4) with, for instance, an increase in northern African precipitation and a decrease in South and East Asian precipitation, through shifts of the atmospheric circulation. The 1980–2014 trend in NHLM precipitation is not significantly affected by natural external forcings (Fig. 3j).

## 4. Trends in precipitation, wind, and temperature

Section 4 focuses on trends in regional summer monsoon precipitation. We assess drivers of summer monsoon precipitation trends and assess regional trends in temperature and the lower-tropospheric circulation.

### a. Observations: 1950–80

In the 1970s and 1980s a large drought hit the Sahel (Nicholson 2013), through a weakening of the low-level westerlies and moisture flux convergence (Fig. 4a). The decrease in northern African precipitation is associated with a southward shift of the intertropical convergence zone (ITCZ) over the Atlantic Ocean (Knight et al. 2006). Precipitation decreases over eastern India from 1950 to 1980, through a weakening of the Indian monsoon circulation (Fig. 4a) (Huang et al. 2020). Over the same period, precipitation decreases over eastern



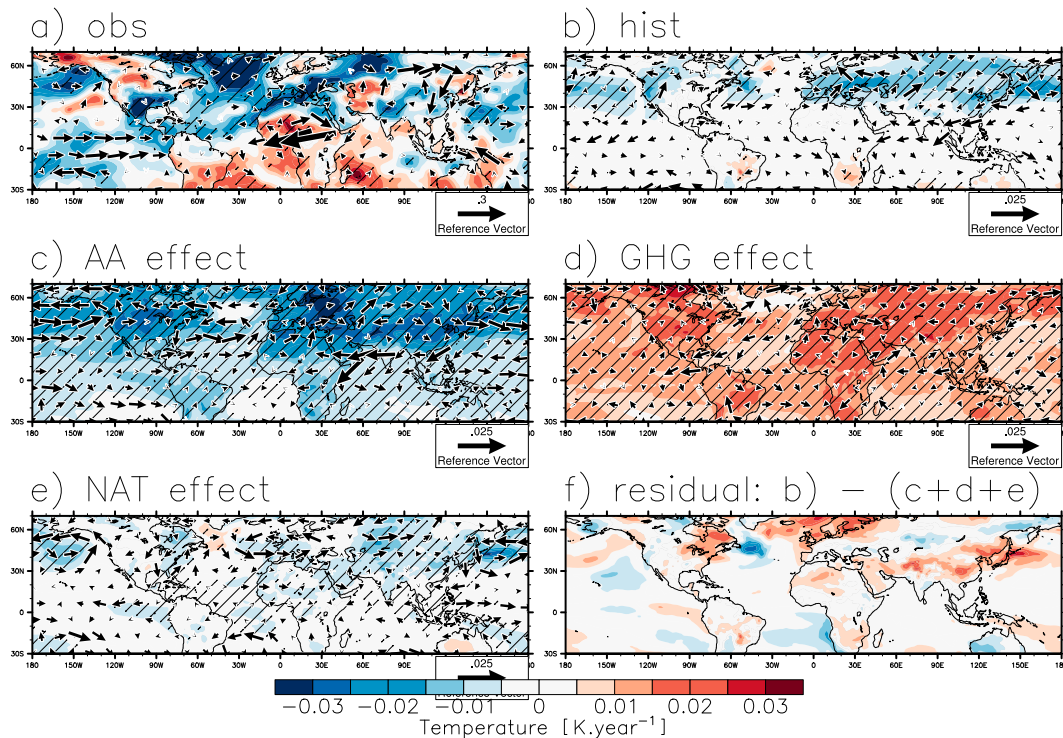


FIG. 5. Trends in surface air temperature ( $\text{K yr}^{-1}$ ; colors) and 850-hPa wind ( $\text{m s}^{-1} \text{yr}^{-1}$ ; arrows) from 1950 to 1980 in MJJAS. Trends are shown for each grid point (a) for the ensemble mean of the (b) historical, (c) hist-AER, (d) hist-GHG, and (e) hist-NAT, and (f) for the residual between the historical simulations and the sum of all forcings. Stippling indicates that precipitation trends are significant at the 95% confidence level according to Student's  $t$  test.

China, due to a weakening of the southwesterly monsoon flow (Fig. 4a).

The observed weakening of the interhemispheric temperature gradient (Friedman et al. 2013) causes monsoon circulations to weaken globally (Fig. 5a) and to shift southward (Figs. 3a and 4a). These changes are due to a decrease in the southward cross-equatorial energy flux that can be interpreted as a southward shift of the Hadley circulation, as shown in Biasutti et al. (2018). The aforementioned anomalies result in a decrease in large-scale monsoon precipitation (Fig. 4a). Regional changes in temperature also contribute to the negative trend in precipitation. The cooling of the North Atlantic temperature is reminiscent of a negative phase of the Atlantic multidecadal variability (AMV) (Knight et al. 2006; Krishnamurthy and Krishnamurthy 2014; Luo et al. 2018; Monerie et al. 2019). The negative phase of the AMV and anomalously cold Mediterranean SSTs (Fig. 5a) have been associated with a weakening of the atmospheric circulation over West Africa, and with a decrease in Sahel precipitation (Martin and Thorncroft 2014; Rowell 2003; Park et al. 2016; Fontaine et al. 2011). The weakening of the land–sea thermal gradient, with a stronger decrease in surface air temperature over the subtropical Asian latitudes than over the Indian Ocean, also contributes to push the monsoon circulation southward (Fig. 5a) (Jin and Wang 2017).

#### b. CMIP6 simulations: 1950–80

CMIP6 models simulate a moderate 1950–80 drying trend over northern Africa, with a weakening of the westerlies over the tropical Atlantic Ocean and West Africa (Fig. 4b). All models underestimate the drying trend over northern Africa, and the low values shown in Fig. 4b are not the result of cancellations in the MMM (Fig. S5). Models simulate a drying over eastern India, and substantial drying over Southeast Asia, in line with a weakening of the southwesterlies (Fig. 4b). CMIP6 climate models are therefore able to reproduce changes in observed precipitation over several monsoon domains. However, the models do not reproduce the large observed increase in Amazonian precipitation (Fig. 4b). We relate the decrease in NHLM and its NAF, SAS, and EAS subdomains to the decrease in surface air temperature over Europe and Asia, and to the weakening of the interhemispheric temperature contrast (Fig. 5b).

Single-forcing simulations reveal that increases in AA emissions are associated with a southward shift of the ITCZ, and with a drying over northern Africa, India, and East China, along with a weakening of the low-level winds (Fig. 4c and Fig. S4). AA emissions are associated with a strong cooling of the Northern Hemisphere, weakening the interhemispheric temperature contrast [as also seen in Friedman et al. (2020)], and weakening the monsoon circulations (Ackerley et al.



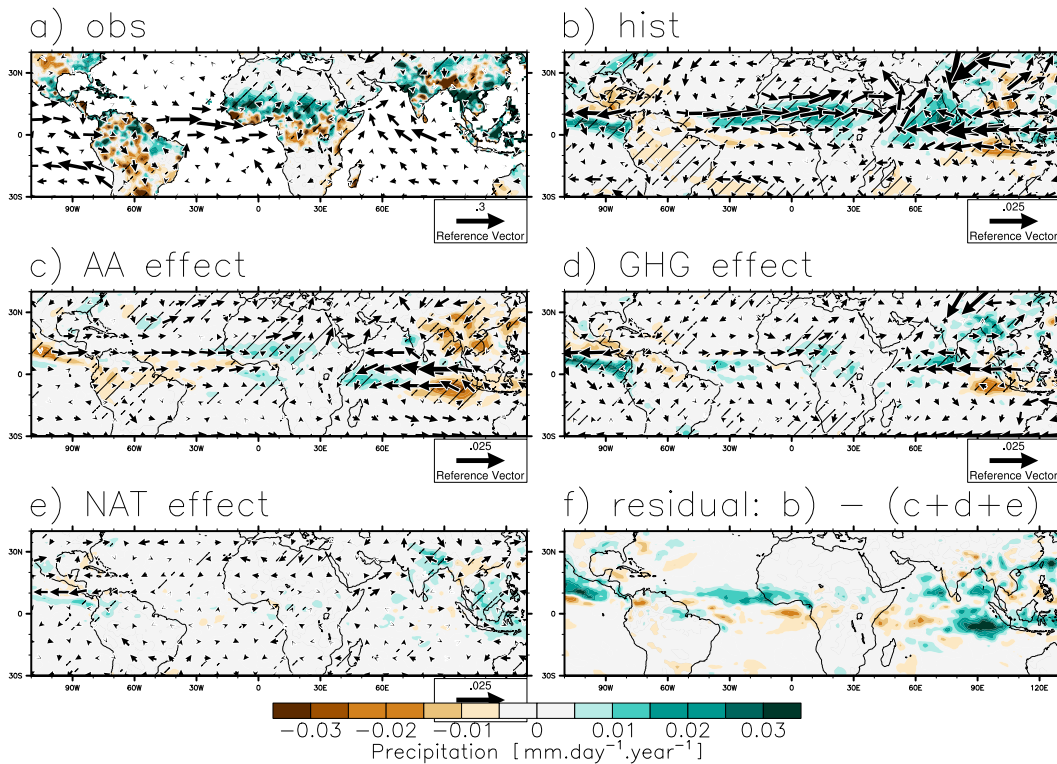


FIG. 6. As in Fig. 4, but for the 1980–2014 trends.

2011; Wang et al. 2012) (Fig. 5c). In addition, the large-scale cooling induced by AA emissions reduces moisture advection, decreasing precipitation over the tropics (Fig. 3e).

The increase in GHG concentrations affects East Indian and Chinese precipitation (Fig. 4d) and the tropical Atlantic Ocean. The increase in GHGs is associated with an increase in surface air temperature, and a strengthening of the large-scale land–sea thermal contrast, explaining a strengthening of the low-level westerlies over the Indian Ocean (Fig. 5d) and the increase in Indian precipitation.

Natural forcing does not lead to significant changes in tropical precipitation, except over northeast China, where an increase in precipitation is seen (Fig. 4e). Natural forcing is also associated with a cooling over the north and the eastern Pacific Ocean and the tropical South Atlantic Ocean, suggesting forcing by the solar cycle and volcanic activity on Pacific and Atlantic SSTs (Fig. 5e), as proposed in Meehl et al. (2009). Natural forcing also leads to a surface cooling over East Asia and China. While we show no strong effects of natural forcing on decadal trends in summer monsoon precipitation, we acknowledge that previous studies have shown substantial effects of the volcanic activity, with reduced precipitation over the Northern Hemisphere in the year that follows specific volcanic eruptions (Haywood et al. 2013; Liu et al. 2016; Jacobson et al. 2020; Herman et al. 2020). We show interannual anomalies in summer monsoon precipitation associated with the NAT effect (Fig. S6) and confirm effects of El Chichón (1982) and

Pinatubo (1991) on NHLM and NAF summer monsoon precipitation, as shown in Herman et al. (2020).

In summary, we suggest that the observed drying of the NH is associated with the increase in global AA emissions, which is the dominant driver of the weakening of the interhemispheric temperature contrast (offsetting the GHG effect) (Friedman et al. 2013, 2020; Polson et al. 2014; Allen et al. 2015). The effect of AA emissions on the interhemispheric temperature contrast allows circulation to shift (Fig. 3e) and the large-scale cooling is associated with a weakening in moisture advection (Fig. 3e). However, we show further in Figs. 4f and 5f that the decomposition of the AA, GHG, and NAT forcings does not account for the full response of historical simulations, with a residual that has a magnitude comparable to the historical trends. Therefore, we acknowledge that one cannot fully quantify the respective effects of AA, GHG, and NAT forcings from the historical CMIP6 model simulations and their DAMIP counterparts.

### c. Observations: 1980–2014

West African monsoon precipitation experienced a limited recovery after the drought of the 1970s and 1980s (Fig. 6a; Sanogo et al. 2015), along with a strengthening of the westerlies and a northward shift of the monsoon circulation (Fig. 6a). Precipitation decreased over South America, in line with a weakening of the easterlies and a northward shift of the ITCZ over the Atlantic Ocean (Knight et al. 2006). Observed

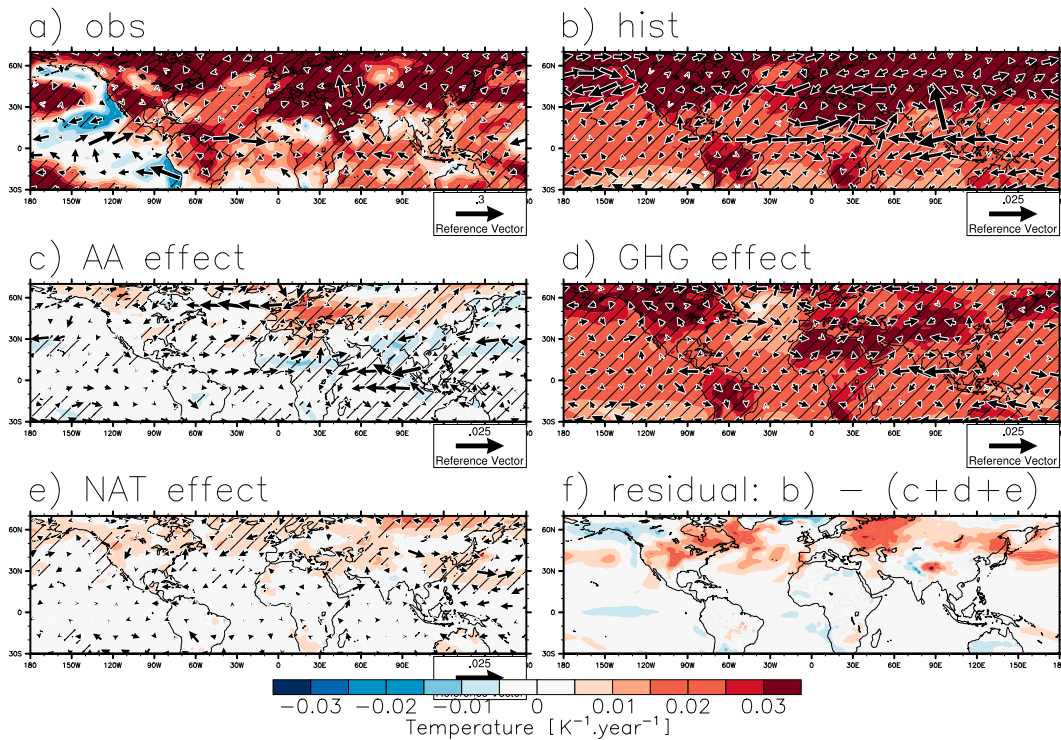


FIG. 7. As in Fig. 5, but for the 1980–2014 trends.

precipitation increased over northern India and much of East Asia (Fig. 6a) through a strengthening of the low-level winds.

The observed temperature increased strongly over the Northern Hemisphere, strengthening the land–sea and inter-hemispheric thermal contrasts and pushing the monsoon

circulation northward (Jin and Wang 2017; Wang et al. 2012) (Fig. 7a). In addition, internal variability (negative phase of the IPO and positive phase of the AMV; Fig. 7a) has contributed to the increase in Sahel and Indian precipitation (Huang et al. 2020; Monerie et al. 2019).

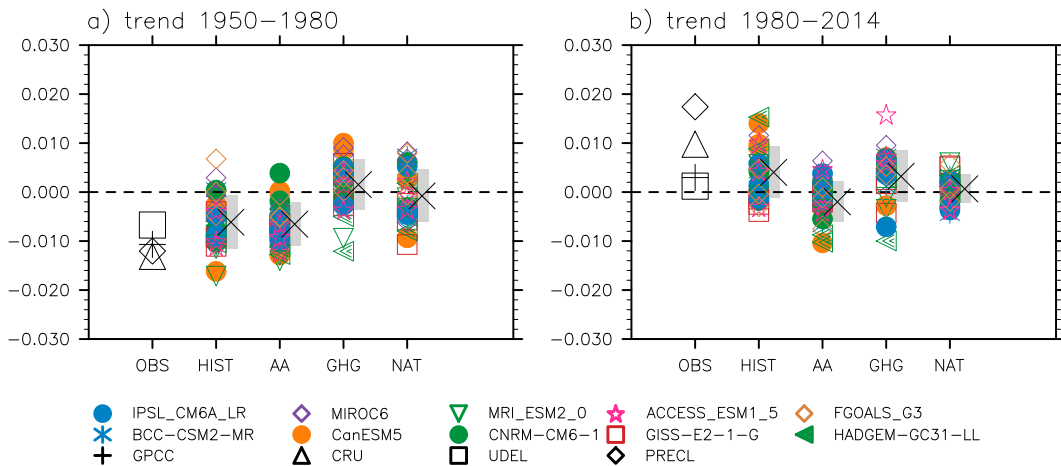


FIG. 8. Trends in NHLM precipitation ( $\text{mm day}^{-1} \text{yr}^{-1}$ ) over the periods (a) 1950–80 and (b) 1980–2014, in MJJAS. Four observations are used: GPCC, CRU, UDEL, and PRECL. The black cross indicates the CMIP6 ensemble mean for the historical simulations (HIST), the anthropogenic aerosols-only simulations (AA), GHG-only simulations (GHG), and natural forcings-only simulations (NAT). The gray shading indicates the spread, defined from the ensemble standard deviation. A different marker is used for each model and all simulated trends are displayed (three members for each model).

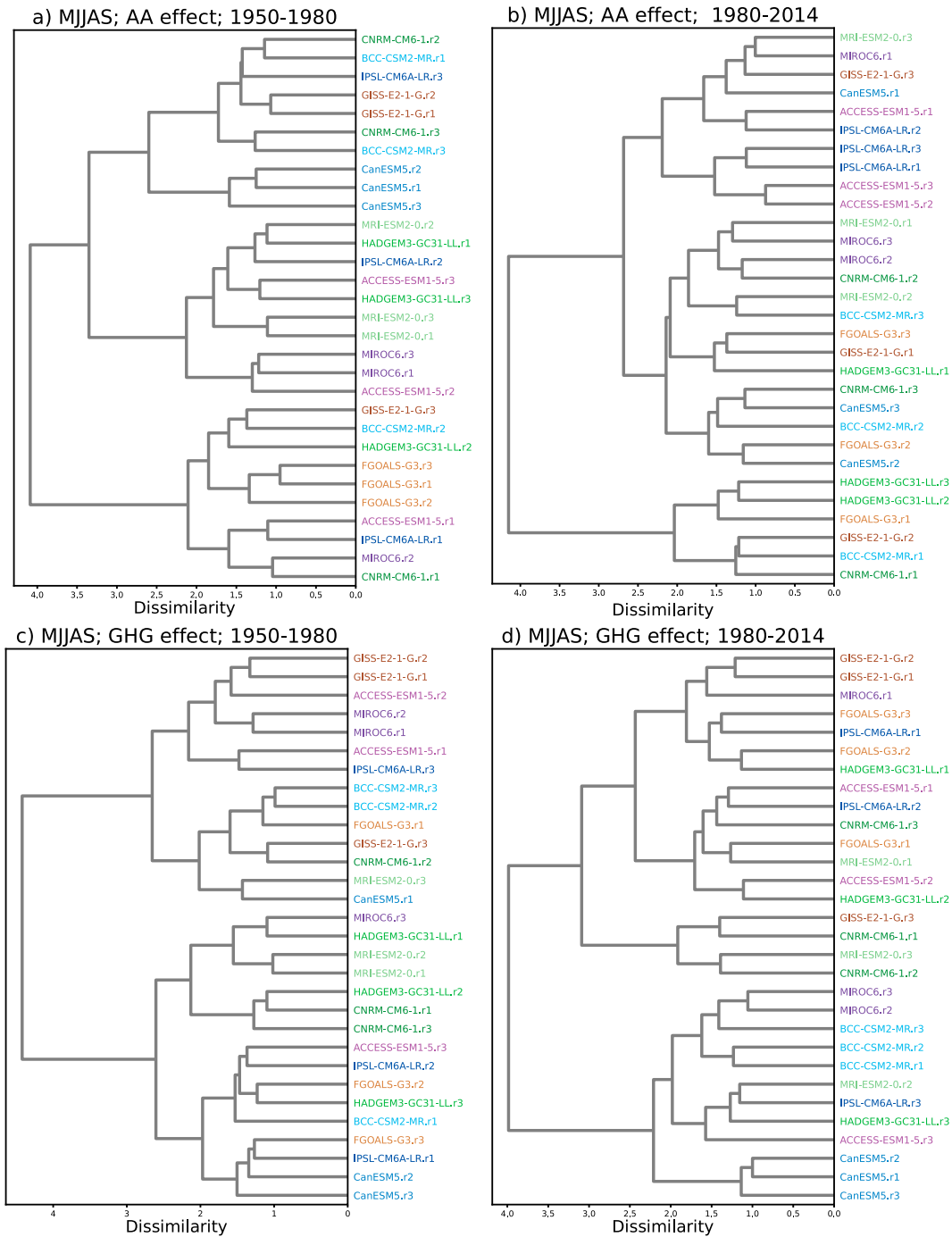


FIG. 9. Model dendrogram from CMIP6 simulations on the MJJAS trends in the (left) 1950–80 and (right) 1980–2014 periods that are associated with (a),(b) AA effect and (c),(d) GHG effect (eight models and three members for each model). Results are shown as a dendrogram [a hierarchical clustering of the pairwise distance matrix for precipitation; see section 2c(4)]. Simulations on the same branch simulate similar patterns in precipitation changes. Each model is shown with a color. In model names, r1, r2, and r3 indicate the first, second and third ensemble member used, respectively, for each model.

d. CMIP6 simulations: 1980–2014

Climate models simulate an increase in NHLM precipitation since 1980 (Fig. 2a), with a strengthening of both northern African and Asian monsoon circulations (Fig. 6b) because

of a strengthening of the interhemispheric temperature contrast (Fig. 7b).

The increase in land–sea thermal contrast is due to the increase in GHG concentrations (Fig. 7d), allowing both

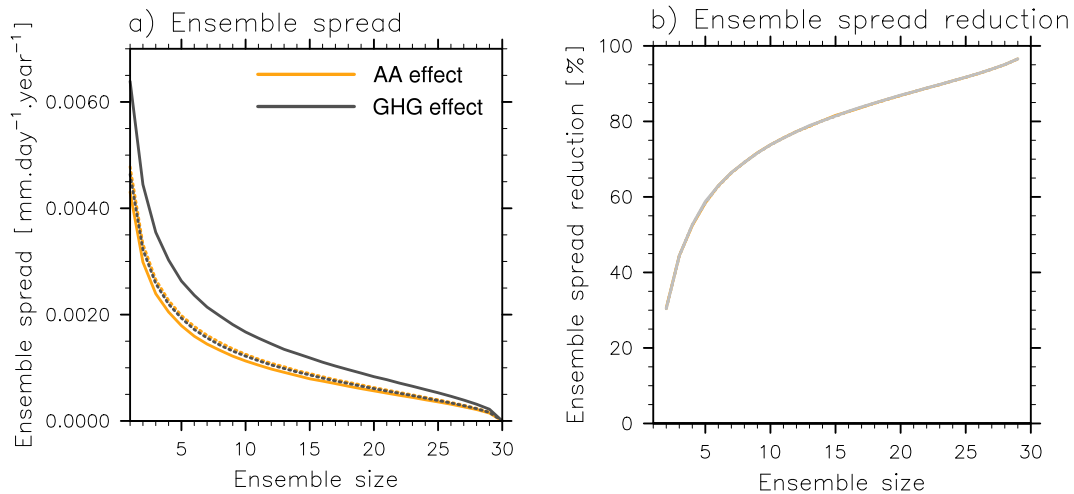


FIG. 10. (a) Spread in precipitation trends (standard deviation; in  $\text{mm}\cdot\text{day}^{-1}\cdot\text{yr}^{-1}$ ) defined from the ensemble means of 100 000 ensembles of  $n$  members from the CanESM5 large ensemble, with  $n$  ranging from 1 to 30. (b) Reduction in the spread (in %), relative to the spread across 100 000 ensembles of 1 member. The  $n$  members are selected randomly in a Monte Carlo approach and selected from CanESM5, using 100 000 permutations. Results are given for the AA effect (orange) and GHG effect (gray) single-forcing experiments and for both 1950–80 (continuous line) and 1980–2014 periods (dotted line).

Indian and northern West African monsoon precipitation to increase (Fig. 6d), as seen in the context of a warming climate (Sandeep and Ajayamohan 2015; Chadwick et al. 2019). The decrease in European AA emissions is associated with an increase in NAF precipitation (Fig. 6c), due to a warming over Europe and the Mediterranean Sea (Fig. 7c), which allows the northerlies to strengthen (Fig. 1b), as documented in Dong et al. (2016a) and Park et al. (2016). The increase in Indian and Chinese AA emissions (Fig. 1b) is associated with cooling over land (through reducing the net surface radiative heat flux; not shown), weakening of the land–sea thermal contrast, weakening the low-level wind (Fig. 7c), and reducing precipitation (Fig. 6c) (Bollasina et al. 2011, among others). We note a strengthening of the 850-hPa wind over the equatorial and northern Indian Ocean in both observation (Fig. 6a) and CMIP6 historical simulations (Fig. 6b). The strengthening of the 850-hPa wind over the equatorial and northern Indian Ocean is due to both the reduction in AA emissions (Fig. 6c) and the increase in GHG concentration (Fig. 6d). The reduction in AA emissions is associated with a strengthening of the northerlies, from the eastern Indian Ocean to western India, favoring precipitation over western India (Fig. 6c). The strengthening of the Indian equatorial easterlies is associated with both changes in large-scale circulation and with enhancement and suppression of deep convection over the western and eastern Indian Ocean, respectively (not shown).

Changes in natural forcing are associated with a significant increase in precipitation over northern India (Fig. 6e), because of a warming of the Asian subtropics (Fig. 7e).

In summary, we note that the single-forcing simulations suggest that the simulated recovery in NAF precipitation is due to a combination of AA and GHG forcing with a large contribution from the residual term, while the East Asian drying is

dominated by AA. The Indian precipitation increase appears to be mainly the result of GHG and NAT forcing. Trends are statistically significant, showing robust AA and GHG effects on monsoon precipitation throughout the twentieth century. However, just as for the 1950–80 period, the single forcing simulations do not account for the full magnitude of trends found in the historical simulations (Figs. 6f and 7f).

## 5. Uncertainties in precipitation trends

We found a large intermodel spread in trends in NHLM precipitation components (Fig. 3). We explore in this section the causes of uncertainty in simulating effects of external forcings on monsoon precipitation.

### a. Total uncertainty across the CMIP6 ensemble

Figure 8 shows trends in NHLM precipitation for each ensemble member of each model. CMIP6 climate models successfully simulate trends in NHLM precipitation of similar intensity to the observations, exhibiting a drying from 1950 to 1980 (Fig. 8a) and getting wetter from 1980 to 2014 (Fig. 8b). However, uncertainties are high for each period and for the effects of each forcing, and individual model realizations can show either increases or decreases in precipitation, so that some ensemble members produce trends of opposite sign to the observations. The magnitude of the observed trends in precipitation are also dependent on the observational datasets used, particularly for 1980–2014. We note that uncertainties are stronger when considering the regional monsoon domains, because the Northern Hemisphere area average reduces the intermodel spread (Fig. S5).

Uncertainty in the effects of anthropogenic factors could arise due to differences in model formulations (Wilcox et al. 2015), including their representations of aerosol–cloud

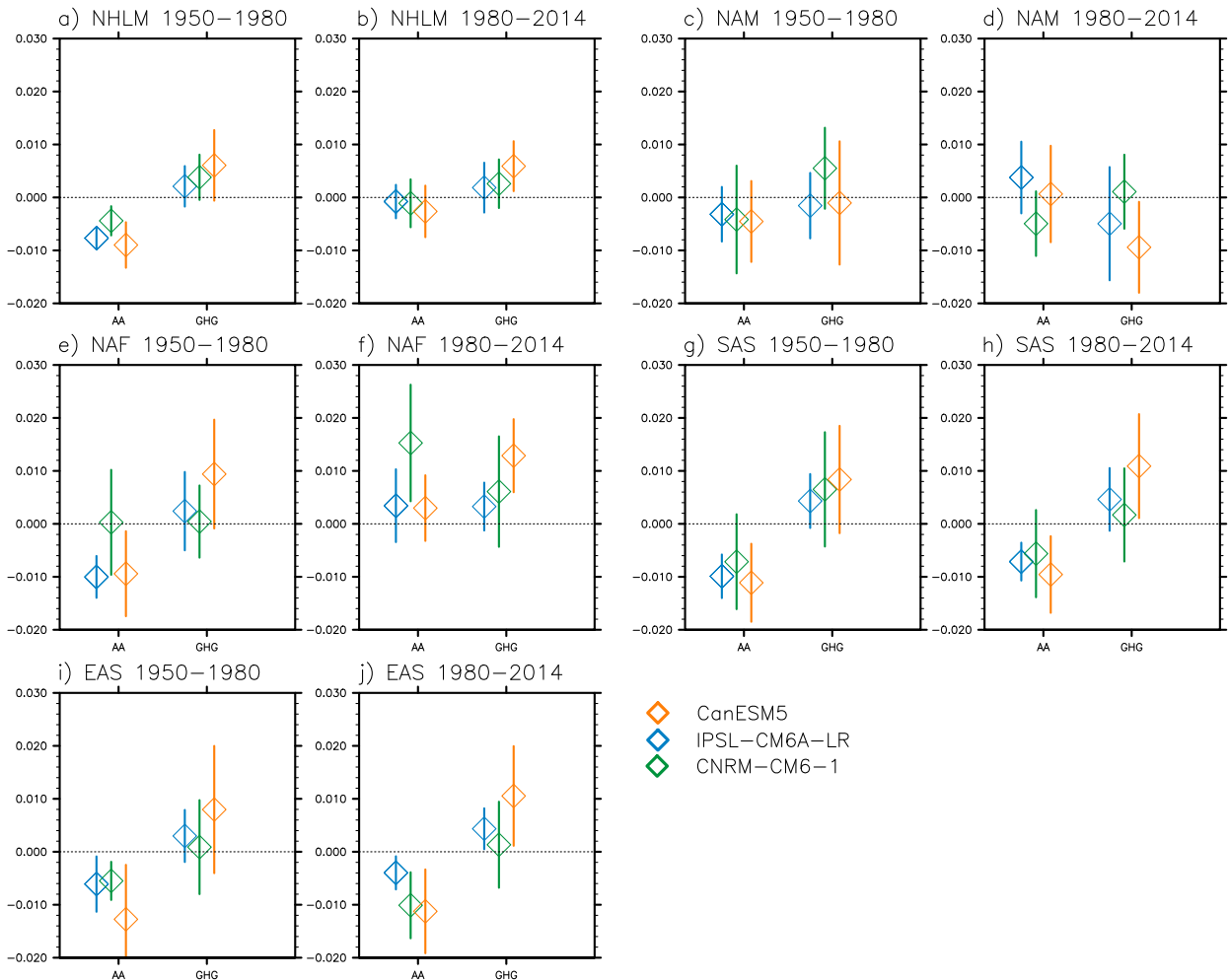


FIG. 11. Ensemble-mean in precipitation trends ( $\text{mm day}^{-1} \text{yr}^{-1}$ ) in MJJAS for (a),(b) NHLM, (c),(d) NAM, (e),(f) NAF, (g),(h) SAS, and (i),(j) EAS monsoon domains, associated with the AA and GHG effects. Trends are computed over the periods (a),(c),(e),(g),(i) 1950–80 and (b),(d),(f),(h),(j) 1980–2014. The marker indicates the ensemble mean and the vertical lines the ensemble standard deviation. Results are given for three models: CNRM-CM6-1 (green; 10 members), IPSL-CM6A-LR (blue; 10 members), and CanESM5 (orange; 30 members).

interactions and aerosol–radiation interactions, which affect both the magnitude and distribution of forcing. Uncertainty could also be due to the effects of internal climate variability, which is expected not to be in phase between simulations, leading to differences between simulations in trends in precipitation.

#### b. A strong effect of internal variability across the CMIP6 ensemble

We verify whether results are model-dependent (i.e., whether the uncertainty is due to the model uncertainty), or not (i.e., uncertainty is due to the internal climate variability uncertainty), by grouping simulations according to their patterns of precipitation change. We classified trends in monsoon precipitation using a hierarchical clustering algorithm [see section 2c(4)]. In the dendrogram, the position at which two simulations are connected explains their degree of similarity

in patterns of monsoon precipitation trend agreement (Fig. 9).

We first describe the results for the AA effect over the period 1950–80. Figure 9a shows that all ensemble members of CanESM5 are in a single cluster, and all ensemble members of FGOALS-G3 are also in a single cluster, but different from CanESM5. Therefore, we can conclude that differences in precipitation trends between CanESM5 and FGOALS-G3 are unlikely to be due to internal climate variability, but rather result from differences in model formulation.

However, one cannot clearly see differences between most of the climate models (e.g., CNRM-CM-1, IPSL-CM6A-LR, BCC-CSM2-MR) due to the effects of internal climate variability. We reach a similar conclusion for the period 1980–2014 but note that the exact structure of the dendrogram is sensitive to the period we have used (Fig. 9b). The same picture is drawn when also considering the GHG effect,



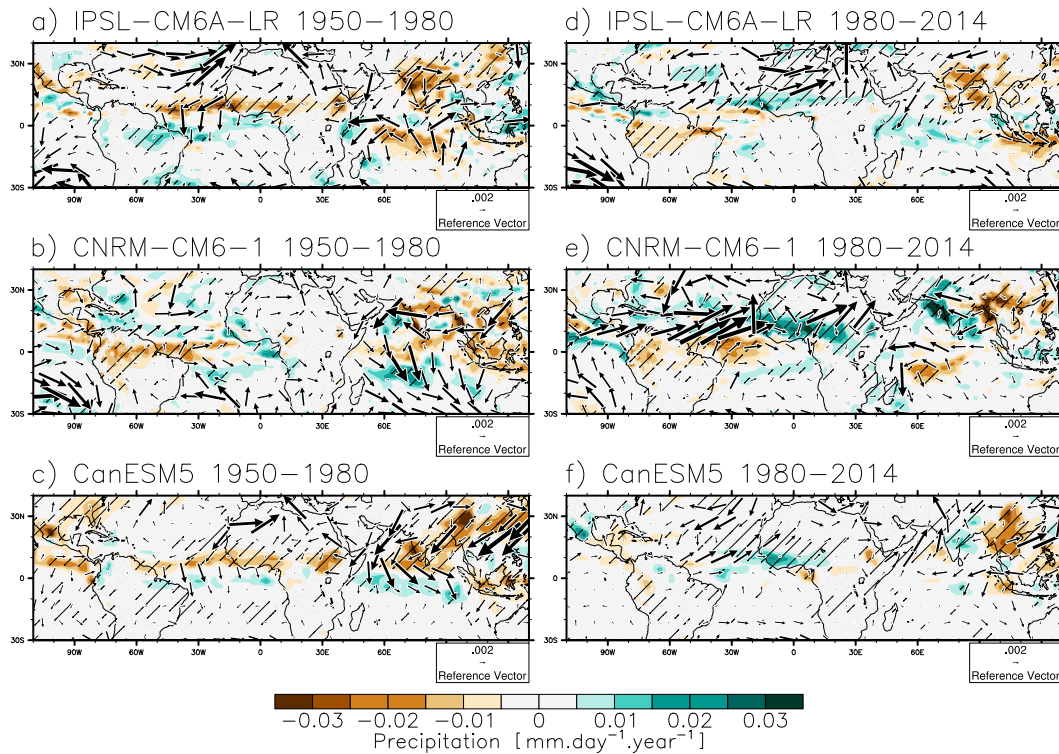


FIG. 12. Trends in precipitation ( $\text{mm day}^{-1} \text{yr}^{-1}$ ; colors) and surface wind ( $\text{m s}^{-1} \text{yr}^{-1}$ ; arrows) in MJJAS in hist-AER. Trends are shown for (a) IPSL-CM6A-LR, (b) CNRM-CM6-1, and (c) CanESM5 ensemble means, for the period 1950–80. (d)–(f) As in (a)–(c), but for the period 1980–2014. Hatching indicates that precipitation trends are significant at the 95% confidence level according to Student's  $t$  test.

and over both periods (Figs. 9c,d). This result highlights that a large portion of the full uncertainty in precipitation shown in Fig. 8 is due to internal climate variability.

### c. Model uncertainty

#### 1) DEFINING A LARGE ENSEMBLE

Each model realization produces internal climate variability, but this variability is unlikely to be in phase across a number of ensemble members. Therefore, the ensemble mean reduces the effects of internal climate variability on our results (Deser et al. 2012). SMILEs thus allow a more faithful representation of the true variance explained by internal variability, while the ensemble can allow assessment of the effects of external forcing on an individual model. However, in CMIP6 only a limited number of DAMIP ensemble members are available for most of the climate models (i.e., a maximum of three members), while 10 simulations are available for IPSL-CM6A-LR and CNRM-CM6-1, and 30 simulations for CanESM5, and for both hist-AER and hist-GHG simulations.

For further analysis we first assess the minimum ensemble size that is required to extract the AA effects on NHLM precipitation. To do so, we make use of the largest ensemble (CanESM5) to resample trends in NHLM precipitation, randomly defining an ensemble of  $n$  members (with  $n$  ranging from 1 to 30), with 100 000 permutations. Results show that

the inter-ensemble spread is reduced when the ensemble size is increased (i.e., by increasing  $n$ ) (Fig. 10a). The ensemble spread of ensembles of three ensemble members is relatively high. Therefore, using only three ensemble members is expected to provide a misleading representation of the AA and GHG effects on monsoon precipitation (Fig. 10a) for a given model. The inter-ensemble spread decreases less strongly when increasing the ensemble size once  $n > 10$  (Fig. 10a). An ensemble of 10 simulations enables a reduction of the inter-ensemble spread by up to 75% (Fig. 10b), compared to ensembles of only one simulation, increasing confidence in extracting the forced response to AA and GHG simulated by a model. We hence use the climate models for which at least 10 simulations are available, judging them to have large enough ensembles to provide a fair representation of ensemble spread and of AA and GHG effects (i.e., CanESM5, IPSL-CM6A-LR, and CNRM-CM6-1).

#### 2) MODEL UNCERTAINTY IN MONSOON PRECIPITATION TRENDS

We confirm that the decrease in NLHM, SAS, and EAS precipitation due to the increase in AA emissions is robust in individual climate models (Figs. 11a,b,g-j). However, NAF (Fig. 11f) and NAM precipitation trends are uncertain (Fig. 11d) because of high intermodel differences. The effects of GHG are almost always associated with an increase in

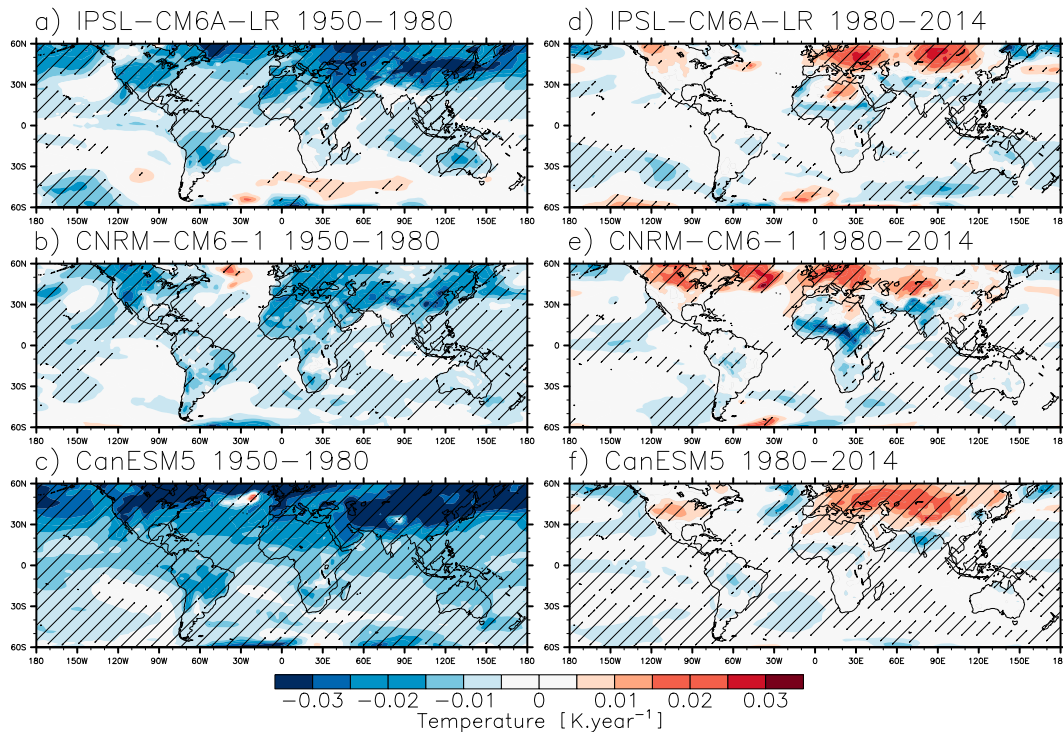


FIG. 13. As in Fig. 12, but for surface air temperature ( $\text{K yr}^{-1}$ ).

precipitation (e.g., NHLM, NAF, SAS, and EAS; Fig. 11), but with no change or a decrease in precipitation over North America (Figs. 11c,d).

The magnitude of internal climate variability is similar in CanESM5 to the other models, suggesting that a reduced ensemble of 10 members is potentially able to well capture this behavior. The ensemble spread is high for each model and each monsoon domain, showing a strong effect of internal climate variability on the simulated trends in precipitation. For NHLM precipitation, differences between models are not substantially stronger than internal climate variability (Figs. 11a,b). In addition to documenting the model uncertainty, SMILEs and single forcings experiments provide the opportunity to address the origin of the trends in monsoon precipitation. Figure 11 shows that the AA effect is stronger than internal climate variability (as seen by an ensemble mean that is stronger than the inter-ensemble spread), suggesting a strong control of AA emissions on the observed 1950–80 drying trend in NHLM, SAS, and EAS precipitation. However, the GHG effect is more uncertain, not exceeding the ensemble spread.

Over the NAF monsoon domain, CNRM-CM6-1 is an outlier in simulating effects of AA emissions, producing no change in precipitation over the period 1950–80 (Fig. 11e) and a strong change in precipitation over the period 1980–2014 (Fig. 11f). Unlike IPSL-CM6A-LR and CanESM5 (Figs. 12a,c), CNRM-CM6-1 does not simulate a southward shift of the ITCZ over West Africa and over the period 1950–80 (Fig. 12b), explaining the moderate change in NAF precipitation

(Fig. 11e). We suggest this reduced shift of ITCZ location to be due to the cooling of the tropical Atlantic Ocean in CNRM-CM6-1 and that, unlike the other models, CNRM-CM6-1 does not produce a weakening of the cross-equatorial Atlantic temperature contrast (Figs. 13a–c), which is one of the drivers of the West African monsoon (Biasutti 2019). This difference arises from the response of AA emissions to downwelling surface shortwave radiation, which is reduced over the North Atlantic Ocean in both IPSL-CM6A-LR and CanESM5, but whose anomalies are not significant in CNRM-CM6-1 (Fig. S6). Over the period 1980–2014, precipitation increases over northern Africa in all models, but the change is stronger in CNRM-CM6-1 than in the two other models (Fig. 12e), along with a stronger change in the low-level westerlies. We hypothesize that this difference arises from the strong warming of the subtropical North Atlantic Ocean, which is not simulated by the two other models, and which has previously been associated with an increase in northern African precipitation (Dunstone et al. 2011) (Figs. 13d–f). In CNRM-CM6-1, the warming of the extratropical North Atlantic Ocean is associated with a significant increase in downwelling surface shortwave radiation, because of a decrease in AA particles (Fig. S7).

The model uncertainty stands out when considering regional trends in precipitation for each grid point. For instance, the effects of AA emissions on SAS precipitation are relatively similar among models (Fig. 11h), but IPSL-CM6A-LR simulates a strong decrease in precipitation over India (Fig. 12d), while CNRM-CM6-1 simulates a decrease

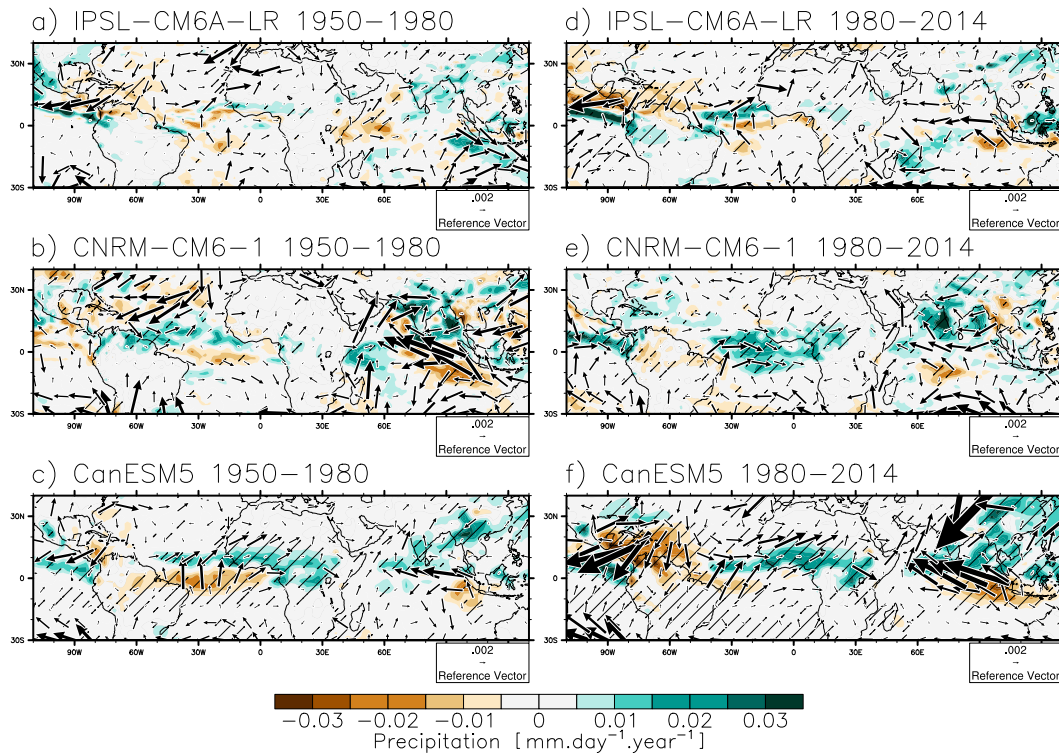


FIG. 14. Trends in precipitation ( $\text{mm day}^{-1} \text{yr}^{-1}$ ; colors) and surface wind ( $\text{m s}^{-1} \text{yr}^{-1}$ ; arrows) in MJJAS in hist-GHG. Trends are shown for (a) IPSL-CM6A-LR, (b) CNRM-CM6-1, and (c) CanESM5 ensemble means, for the period 1950–80. (d)–(f) As in (a)–(c), but for the period 1980–2014. Stippling indicates that precipitation trends are significant at the 95% confidence level, and according to Student's  $t$  test.

over eastern India and southern China (Fig. 12e), and CanESM5 over Southeast Asia only (along with an increase over India) (Fig. 12f).

CanESM5 simulates a stronger effect of GHG on NAF, EAS, and SAS precipitation than do IPSL-CM6A-LR and CNRM-CM6-1 (Figs. 11e,f). This is due to greater strengthening of the low-level wind (Figs. 14c,f) and of the interhemispheric temperature gradient in CanESM5 (Fig. 15).

Section 5 shows that effects of external forcing are model dependent over the NAF and SAS monsoon domains, due to differences in their effects on regional changes in temperature. This stresses the need for a better understanding of the effects of external forcings on monsoon precipitation, and on causes of uncertainties among models.

## 6. Conclusions

We explore the Northern Hemisphere land monsoon precipitation trends over two periods: 1950–80, when global emissions of anthropogenic aerosols rapidly increased, and 1980–2014, when U.S. and western European emissions decreased while Asian emissions continued to increase. Historical CMIP6 simulations were used to assess model performance in simulating the monsoon precipitation, and single forcing simulations from DAMIP (Gillett et al. 2016) were used to quantify the relative influences of anthropogenic

aerosols, greenhouse gases, and natural forcings on the monsoon precipitation trends. We unraveled physical drivers of summer monsoon precipitation trends by decomposing precipitation anomalies into dynamic and thermodynamic components, following Chadwick et al. (2016). This is the first application, to our knowledge, of this decomposition technique for attributing drivers of multidecadal change in the monsoon domains.

While the physical complexity of climate models has increased since CMIP5, CMIP6 models are not appreciably different from CMIP5 models in their simulation of tropical precipitation on different temporal and spatial scales (Fiedler et al. 2020). We showed that models are generally biased dry and underestimate the extent of the monsoon domains. We acknowledge that systematic biases seen in the CMIP6 models is a source of uncertainty for simulating effects of external forcings on monsoon precipitation. This is particularly true for SAS precipitation because of the strong dry bias in Indian precipitation.

We showed that climate models qualitatively reproduce the observed multidecadal evolution of the NHLM precipitation: precipitation decreases from 1950 to 1980 and increases afterward. Although low-frequency variability in monsoon precipitation has previously been associated with internal climate variability (Martin and Thorncroft 2014; Monerie et al. 2019; Huang et al. 2020; Wang et al. 2017), we



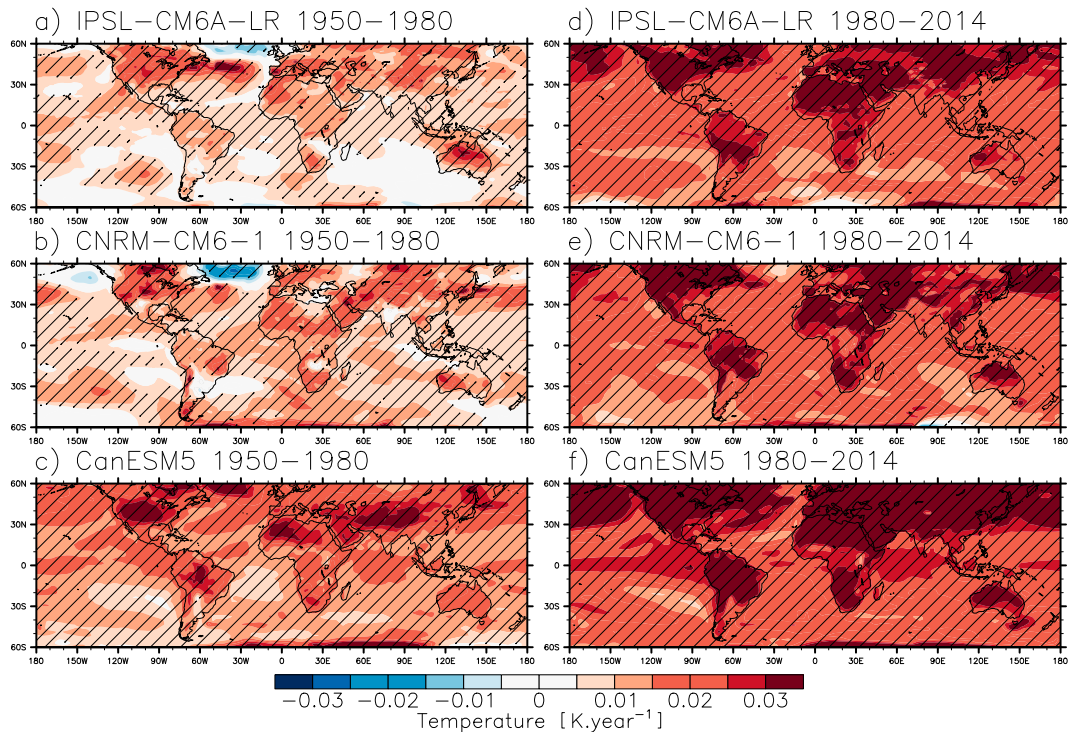


FIG. 15. As in Fig. 14, but for surface air temperature ( $\text{K yr}^{-1}$ ).

show that anthropogenic forcings partly drive decadal trends in NHLM, West African, and Indian monsoon precipitation:

- The decrease in NHLM precipitation is associated with increases in AA emissions, leading to a decrease in precipitation over northern Africa and Asia from 1950 to 1980, through a weakening of the interhemispheric temperature contrast and shifts of the monsoon circulations. The decrease in NHLM precipitation due to AA is partly counteracted by the increase in GHG concentration through an increase in specific humidity and a strengthening of moisture advection.
- The increase in NHLM precipitation is mostly associated with the increase in GHG concentrations because of an increase in global mean surface air temperature and in specific humidity and a strengthening of moisture advection. The moisture advection is partly counteracted by a weakening of the tropical mean circulation.
- After 1980, European anthropogenic aerosol emissions decreased, leading to a substantial increase in NAF precipitation by increasing temperature over northern Africa and the Mediterranean Sea. In the meantime, Asian emissions continued to increase, leading to a decrease in SAS and EAS precipitation, by reducing land-sea contrasts in temperature.
- Both 1950–80 negative and 1980–2014 positive trends in precipitation are mostly due to dynamic changes of the atmospheric circulation, specifically through shifts in the monsoon circulations. After the 1980s, thermodynamic

changes also contribute to the increase in precipitation, through moisture advection over land.

- In addition to the CMIP6 ensemble, we employed three single-model initial-condition large ensembles (SMILEs). SMILEs show that the AA effect emerges from internal climate variability over the period 1950–80. Results suggest that AA emissions are one of the main drivers in NHLM, SAS, and EAS precipitation trends.

Trends in monsoon precipitation are uncertain among climate models. We show, by decomposing precipitation anomalies, that these uncertainties primarily result from the simulation of changes in atmospheric patterns and circulation.

We suggest that the typical ensemble of three members for each climate model, as provided by CMIP6, can lead to an uncertain representation of the true effects of anthropogenic aerosol emissions in a given climate model, as well as underestimating the magnitude of internal variability. Therefore, we stress that SMILEs would be required to capture the response of a climate model to changes in anthropogenic aerosol emissions, and to allow a faithful representation of internal variability. We explore the relative contributions of internal variability and model structural uncertainty using three SMILEs, allowing a first attempt at quantifying model uncertainty in the large ensemble framework: CanESM5, IPSL-CM6A-LR, and CNRM-CM6-1. The three models disagree on the pattern in precipitation change over the tropics. We show these differences to be due to the intermodel spread in temperature trends, due to differences in the effects of AA on changes in downwelling shortwave

radiation over the North Atlantic Ocean. Generally, CanESM5 is more sensitive than IPSL-CM6A-LR and CNRM-CM6-1 to the increase in GHG concentrations and simulates stronger changes in tropical precipitation over both the 1950–80 and 1980–2014 periods. The climate models that participated in DAMIP draw on the same GHG and AA emissions. The fundamental differences noted between climate model simulations (i.e., changes in large-scale temperature gradients and over the tropical Atlantic Ocean and the Indian Ocean) are therefore due to differences in physical parameterizations between climate models.

We show that AA effects on NHLM precipitation emerge between 1950 and 1980, whereas those of GHG are more uncertain. Regionally, the AA effects on SAS and EAS precipitation emerge over the twentieth and early twenty-first century for the majority of models (two out of three SMILEs), while the GHG effects are moderate and do not emerge. We highlight deficiencies in attributing local changes in tropical precipitation to the AA, GHG, and NAT forcing, which could be due to strong nonlinearities between effects of the forcing. However, we show some consistency between SMILEs and the CMIP6 ensemble in their simulated trends in precipitation, showing that AA emissions contribute substantially to decadal trends in monsoon precipitation. AA and GHG effects are model dependent within the CMIP6 ensemble, and we stress the need for a better understanding of differences between climate models at simulating changes in temperature that are due to changes in external forcings, at both regional and global scales. Changes in AA emissions can counteract or exacerbate effects of GHG increases, depending on the time period considered. Reducing the model uncertainty associated with the AA effect could lead to a better estimation of future changes in monsoon precipitation, particularly for the near-term decades in which aerosol emissions are changing rapidly.

*Acknowledgments.* This work was funded by the EMERGENCE project under the Natural Environment Research Council (NERC Grant NE/S004890/1). We acknowledge the World Climate Research Programme's Working Group on Coupled Modelling, which is responsible for CMIP, and we thank the climate modeling groups for producing and making available their model output. For CMIP the U.S. Department of Energy's Program for Climate Model Diagnosis and Intercomparison provides coordinating support and led development of software infrastructure in partnership with the Global Organization for Earth System Science Portals. GPCC and GPCP Precipitation data are provided by the NOAA/OAR/ESRL PSL, Boulder, Colorado, USA, from their Web site at <https://psl.noaa.gov/>. We also thank the three anonymous reviewers for their comments and suggestions.

*Data availability statement.* CMIP6 GCM output is available from public repositories, including <https://esgf-index1.ceda.ac.uk/search/cmip6-ceda/>. GPCC and GPCP Precipitation data are provided by the NOAA/OAR/ESRL PSL, Boulder, Colorado, USA, from their website at <https://psl.noaa.gov/>.

## REFERENCES

- Ackerley, D., B. B. Booth, S. H. E. Knight, E. J. Highwood, D. J. Frame, M. R. Allen, and D. P. Rowell, 2011: Sensitivity of twentieth-century Sahel rainfall to sulfate aerosol and CO<sub>2</sub> forcing. *J. Climate*, **24**, 4999–5014, <https://doi.org/10.1175/JCLI-D-11-00019.1>.
- Allen, R. J., A. T. Evan, and B. B. Booth, 2015: Interhemispheric aerosol radiative forcing and tropical precipitation shifts during the late twentieth century. *J. Climate*, **28**, 8219–8246, <https://doi.org/10.1175/JCLI-D-15-0148.1>.
- Ayantika, D. C., R. Krishnan, M. Singh, P. Swapna, N. Sandeep, A. G. Prajeesh, and R. Vellore, 2021: Understanding the combined effects of global warming and anthropogenic aerosol forcing on the South Asian monsoon. *Climate Dyn.*, **56**, 1643–1662, <https://doi.org/10.1007/s00382-020-05551-5>.
- Biasutti, M., 2019: Rainfall trends in the African Sahel: Characteristics, processes, and causes. *Wiley Interdiscip. Rev.: Climate Change*, **10**, e591, <https://doi.org/doi:10.1002/wcc.591>.
- , and Coauthors, 2018: Global energetics and local physics as drivers of past, present and future monsoons. *Nat. Geosci.*, **11**, 392–400, <https://doi.org/10.1038/s41561-018-0137-1>.
- Bollasina, M. A., Y. Ming, and V. Ramaswamy, 2011: Anthropogenic aerosols and the weakening of the South Asian summer monsoon. *Science*, **334**, 502–505, <https://doi.org/10.1126/science.1204994>.
- Bonfils, C. J. W., B. D. Santer, J. C. Fyfe, K. Marvel, T. J. Phillips, and S. R. H. Zimmerman, 2020: Human influence on joint changes in temperature, rainfall and continental aridity. *Nat. Climate Change*, **10**, 726–731, <https://doi.org/10.1038/s41558-020-0821-1>.
- Bordonì, S., and T. Schneider, 2008: Monsoons as eddy-mediated regime transitions of the tropical overturning circulation. *Nat. Geosci.*, **1**, 515–519, <https://doi.org/10.1038/ngeo248>.
- Boucher, O., and Coauthors, 2020: Presentation and evaluation of the IPSL-CM6A-LR climate model. *J. Adv. Model. Earth Syst.*, **12**, e2019MS002010, <https://doi.org/10.1029/2019MS002010>.
- Cao, J., B. Wang, B. Wang, H. Zhao, C. Wang, and Y. Han, 2020: Sources of the intermodel spread in projected global monsoon hydrological sensitivity. *Geophys. Res. Lett.*, **47**, e2020GL089560, <https://doi.org/10.1029/2020GL089560>.
- Chadwick, R., I. Boutle, and G. Martin, 2013: Spatial patterns of precipitation change in CMIP5: Why the rich do not get richer in the tropics. *J. Climate*, **26**, 3803–3822, <https://doi.org/10.1175/JCLI-D-12-00543.1>.
- , P. Good, and K. Willett, 2016: A simple moisture advection model of specific humidity change over land in response to SST warming. *J. Climate*, **29**, 7613–7632, <https://doi.org/10.1175/JCLI-D-16-0241.1>.
- , D. Ackerley, T. Ogura, and D. Dommenget, 2019: Separating the influences of land warming, the direct CO<sub>2</sub> effect, the plant physiological effect, and SST warming on regional precipitation changes. *J. Geophys. Res. Atmos.*, **124**, 624–640, <https://doi.org/10.1029/2018JD029423>.
- Chen, M., P. Xie, J. E. Janowiak, and P. A. Arkin, 2002: Global land precipitation: A 50-yr monthly analysis based on gauge observations. *J. Hydrometeorol.*, **3**, 249–266, [https://doi.org/10.1175/1525-7541\(2002\)003<0249:GLPAYM>2.0.CO;2](https://doi.org/10.1175/1525-7541(2002)003<0249:GLPAYM>2.0.CO;2).
- Chou, C., and C.-A. Chen, 2010: Depth of convection and the weakening of tropical circulation in global warming. *J. Climate*, **23**, 3019–3030, <https://doi.org/10.1175/2010JCLI3383.1>.



- , T.-C. Wu, and P.-H. Tan, 2013: Changes in gross moist stability in the tropics under global warming. *Climate Dyn.*, **41**, 2481–2496, <https://doi.org/10.1007/s00382-013-1703-2>.
- Collins, W. J., and Coauthors, 2017: AerChemMIP: Quantifying the effects of chemistry and aerosols in CMIP6. *Geosci. Model Dev.*, **10**, 585–607, <https://doi.org/10.5194/gmd-10-585-2017>.
- D'Agostino, R., J. Bader, S. Bordoni, D. Ferreira, and J. Jungclaus, 2019: Northern Hemisphere monsoon response to mid-Holocene orbital forcing and greenhouse gas-induced global warming. *Geophys. Res. Lett.*, **46**, 1591–1601, <https://doi.org/10.1029/2018GL081589>.
- , J. R. Brown, A. Moise, H. Nguyen, P. L. Silva Dias, and J. Jungclaus, 2020: Contrasting Southern Hemisphere monsoon response: Mid-Holocene orbital forcing versus future greenhouse gas-induced global warming. *J. Climate*, **33**, 9595–9613, <https://doi.org/10.1175/JCLI-D-19-0672.1>.
- Deser, C., A. Phillips, V. Bourdette, and H. Teng, 2012: Uncertainty in climate change projections: The role of internal variability. *Climate Dyn.*, **38**, 527–546, <https://doi.org/10.1007/s00382-010-0977-x>.
- Dong, B., and R. Sutton, 2015: Dominant role of greenhouse-gas forcing in the recovery of Sahel rainfall. *Nat. Climate Change*, **5**, 757–760, <https://doi.org/10.1038/nclimate2664>.
- , —, E. Highwood, and L. Wilcox, 2014: The impacts of European and Asian anthropogenic sulfur dioxide emissions on Sahel rainfall. *J. Climate*, **27**, 7000–7017, <https://doi.org/10.1175/JCLI-D-13-00769.1>.
- , —, W. Chen, X. Liu, R. Lu, and Y. Sun, 2016a: Abrupt summer warming and changes in temperature extremes over Northeast Asia since the mid-1990s: Drivers and physical processes. *Adv. Atmos. Sci.*, **33**, 1005–1023, <https://doi.org/10.1007/s00376-016-5247-3>.
- , —, E. J. Highwood, and L. J. Wilcox, 2016b: Preferred response of the East Asian summer monsoon to local and non-local anthropogenic sulphur dioxide emissions. *Climate Dyn.*, **46**, 1733–1751, <https://doi.org/10.1007/s00382-015-2671-5>.
- Dunstone, N. J., D. M. Smith, and R. Eade, 2011: Multi-year predictability of the tropical Atlantic atmosphere driven by the high latitude North Atlantic Ocean. *Geophys. Res. Lett.*, **38**, L14701, <https://doi.org/10.1029/2011GL047949>.
- Eyring, V., S. Bony, G. A. Meehl, C. A. Senior, B. Stevens, R. J. Stouffer, and K. E. Taylor, 2016: Overview of the Coupled Model Intercomparison Project phase 6 (CMIP6) experimental design and organization. *Geosci. Model Dev.*, **9**, 1937–1958, <https://doi.org/10.5194/gmd-9-1937-2016>.
- Fiedler, S., and Coauthors, 2020: Simulated tropical precipitation assessed across three major phases of the Coupled Model Intercomparison Project (CMIP). *Mon. Wea. Rev.*, **148**, 3653–3680, <https://doi.org/10.1175/MWR-D-19-0404.1>.
- Fontaine, B., M. Gaetani, A. Ullmann, and P. Roucou, 2011: Time evolution of observed July–September sea surface temperature–Sahel climate teleconnection with removed quasi-global effect (1900–2008). *J. Geophys. Res.*, **116**, D04105, <https://doi.org/10.1029/2010JD014843>.
- Friedman, A. R., Y.-T. Hwang, J. C. H. Chiang, and D. M. W. Frierson, 2013: Interhemispheric temperature asymmetry over the twentieth century and in future projections. *J. Climate*, **26**, 5419–5433, <https://doi.org/10.1175/JCLI-D-12-00525.1>.
- , G. C. Hegerl, A. P. Schurer, S.-Y. Lee, W. Kong, W. Cheng, and J. C. H. Chiang, 2020: Forced and unforced decadal behavior of the interhemispheric SST contrast during the instrumental period (1881–2012): Contextualizing the late 1960s–early 1970s shift. *J. Climate*, **33**, 3487–3509, <https://doi.org/10.1175/JCLI-D-19-0102.1>.
- Giannini, A., and A. Kaplan, 2019: The role of aerosols and greenhouse gases in Sahel drought and recovery. *Climatic Change*, **152**, 449–466, <https://doi.org/10.1007/s10584-018-2341-9>.
- , R. Saravanan, and P. Chang, 2003: Oceanic forcing of Sahel rainfall on interannual to interdecadal time scales. *Science*, **302**, 1027–1030, <https://doi.org/10.1126/science.1089357>.
- Gillett, N. P., and Coauthors, 2016: The Detection and Attribution Model Intercomparison Project (DAMIP v1.0) contribution to CMIP6. *Geosci. Model Dev.*, **9**, 3685–3697, <https://doi.org/10.5194/gmd-9-3685-2016>.
- Guo, L., E. J. Highwood, L. C. Shaffrey, and A. G. Turner, 2013: The effect of regional changes in anthropogenic aerosols on rainfall of the East Asian summer monsoon. *Atmos. Chem. Phys.*, **13**, 1521–1534, <https://doi.org/10.5194/acp-13-1521-2013>.
- , A. G. Turner, and E. J. Highwood, 2016: Local and remote impacts of aerosol species on Indian summer monsoon rainfall in a GCM. *J. Climate*, **29**, 6937–6955, <https://doi.org/10.1175/JCLI-D-15-0728.1>.
- Harris, I., P. D. Jones, T. J. Osborn, and D. H. Lister, 2014: Updated high-resolution grids of monthly climatic observations—The CRU TS3.10 dataset. *Int. J. Climatol.*, **34**, 623–642, <https://doi.org/10.1002/joc.3711>.
- Haywood, J. M., A. Jones, N. Bellouin, and D. Stephenson, 2013: Asymmetric forcing from stratospheric aerosols impacts Sahelian rainfall. *Nat. Climate Change*, **3**, 660–665, <https://doi.org/10.1038/nclimate1857>.
- Held, I. M., and B. J. Soden, 2006: Robust responses of the hydrological cycle to global warming. *J. Climate*, **19**, 5686–5699, <https://doi.org/10.1175/JCLI3990.1>.
- Herman, R. J., A. Giannini, M. Biasutti, and Y. Kushnir, 2020: The effects of anthropogenic and volcanic aerosols and greenhouse gases on twentieth century Sahel precipitation. *Sci. Rep.*, **10**, 12203, <https://doi.org/10.1038/s41598-020-68356-w>.
- Hirasawa, H., P. J. Kushner, M. Sigmond, J. Fyfe, and C. Deser, 2020: Anthropogenic aerosols dominate forced multidecadal Sahel precipitation change through distinct atmospheric and oceanic drivers. *J. Climate*, **33**, 10187–10204, <https://doi.org/10.1175/JCLI-D-19-0829.1>.
- Huang, X., T. Zhou, W. Zhang, J. Jiang, P. Li, and Y. Zhao, 2019: Northern Hemisphere land monsoon precipitation changes in the twentieth century revealed by multiple reanalysis datasets. *Climate Dyn.*, **53**, 7131–7149, <https://doi.org/10.1007/s00382-019-04982-z>.
- , and Coauthors, 2020: The recent decline and recovery of Indian summer monsoon rainfall: Relative roles of external forcing and internal variability. *J. Climate*, **33**, 5035–5060, <https://doi.org/10.1175/JCLI-D-19-0833.1>.
- Hwang, Y.-T., D. M. W. Frierson, and S. M. Kang, 2013: Anthropogenic sulfate aerosol and the southward shift of tropical precipitation in the late 20th century. *Geophys. Res. Lett.*, **40**, 2845–2850, <https://doi.org/10.1002/grl.50502>.
- Jacobson, T. W., W. Yang, G. A. Vecchi, and L. W. Horowitz, 2020: Impact of volcanic aerosol hemispheric symmetry on Sahel rainfall. *Climate Dyn.*, **55**, 1733–1758, <https://doi.org/10.1007/s00382-020-05347-7>.
- Jain, A. K., M. N. Murty, and P. J. Flynn, 1999: Data clustering: A review. *ACM Comput. Surv.*, **31**, 264–323, <https://doi.org/10.1145/331499.331504>.
- Jin, Q., and C. Wang, 2017: A revival of Indian summer monsoon rainfall since 2002. *Nat. Climate Change*, **7**, 587–594, <https://doi.org/10.1038/nclimate3348>.

- Kanamitsu, M., W. Ebisuzaki, J. Woollen, S.-K. Yang, J. J. Hnilo, M. Fiorino, and G. L. Potter, 2002: NCEP–DOE AMIP-II Reanalysis (R-2). *Bull. Amer. Meteor. Soc.*, **83**, 1631–1644, <https://doi.org/10.1175/BAMS-83-11-1631>.
- Karmalkar, A. V., R. S. Bradley, and H. F. Diaz, 2011: Climate change in Central America and Mexico: Regional climate model validation and climate change projections. *Climate Dyn.*, **37**, 605–629, <https://doi.org/10.1007/s00382-011-1099-9>.
- Kelley, M., and Coauthors, 2020: GISS-E2.1: Configurations and climatology. *J. Adv. Model. Earth Syst.*, **12**, e2019MS002025, <https://doi.org/10.1029/2019MS002025>.
- Kent, C., R. Chadwick, and D. P. Rowell, 2015: Understanding uncertainties in future projections of seasonal tropical precipitation. *J. Climate*, **28**, 4390–4413, <https://doi.org/10.1175/JCLI-D-14-00613.1>.
- Kitoh, A., H. Endo, K. Krishna Kumar, I. F. A. Cavalcanti, P. Goswami, and T. Zhou, 2013: Monsoons in a changing world: A regional perspective in a global context. *J. Geophys. Res. Atmos.*, **118**, 3053–3065, <https://doi.org/10.1002/jgrd.50258>.
- Knight, J. R., C. K. Folland, and A. A. Scaife, 2006: Climate impacts of the Atlantic multidecadal oscillation. *Geophys. Res. Lett.*, **33**, L17706, <https://doi.org/10.1029/2006GL026242>.
- Krishnamurthy, L., and V. Krishnamurthy, 2014: Influence of PDO on South Asian summer monsoon and monsoon–ENSO relation. *Climate Dyn.*, **42**, 2397–2410, <https://doi.org/10.1007/s00382-013-1856-z>.
- Kuhlbrodt, T., and Coauthors, 2018: The low-resolution version of HadGEM3 GC3.1: Development and evaluation for global climate. *J. Adv. Model. Earth Syst.*, **10**, 2865–2888, <https://doi.org/10.1029/2018MS001370>.
- Lee, J.-Y., and B. Wang, 2014: Future change of global monsoon in the CMIP5. *Climate Dyn.*, **42**, 101–119, <https://doi.org/10.1007/s00382-012-1564-0>.
- Li, L., and Coauthors, 2020: The Flexible Global Ocean–Atmosphere–Land System model grid-point version 3 (FGOALS-g3): Description and evaluation. *J. Adv. Model. Earth Syst.*, **12**, e2019MS002012, <https://doi.org/10.1029/2019MS002012>.
- Liu, F., J. Chai, B. Wang, J. Liu, X. Zhang, and Z. Wang, 2016: Global monsoon precipitation responses to large volcanic eruptions. *Sci. Rep.*, **6**, 24331, <https://doi.org/10.1038/srep24331>.
- Luo, F., S. Li, Y. Gao, L. Svendsen, T. Furevik, and N. Keenlyside, 2018: The connection between the Atlantic multidecadal oscillation and the Indian summer monsoon since the industrial revolution is intrinsic to the climate system. *Environ. Res. Lett.*, **13**, 094020, <https://doi.org/10.1088/1748-9326/aade11>.
- Martin, E. R., and C. D. Thorncroft, 2014: The impact of the AMO on the West African monsoon annual cycle. *Quart. J. Roy. Meteor. Soc.*, **140**, 31–46, <https://doi.org/10.1002/qj.2107>.
- Marvel, K., M. Biasutti, and C. Bonfils, 2020: Fingerprints of external forcings on Sahel rainfall: Aerosols, greenhouse gases, and model–observation discrepancies. *Environ. Res. Lett.*, **15**, 084023, <https://doi.org/10.1088/1748-9326/ab858e>.
- Meehl, G. A., J. M. Arblaster, K. Matthes, F. Sassi, and H. van Loon, 2009: Amplifying the Pacific climate system response to a small 11-year solar cycle forcing. *Science*, **325**, 1114–1118, <https://doi.org/10.1126/science.1172872>.
- Monerie, P.-A., E. Sanchez-Gomez, and J. Boé, 2017: On the range of future Sahel precipitation projections and the selection of a sub-sample of CMIP5 models for impact studies. *Climate Dyn.*, **48**, 2751–2770, <https://doi.org/10.1007/s00382-016-3236-y>.
- , J. Robson, B. Dong, D. L. R. Hodson, and N. P. Klingaman, 2019: Effect of the Atlantic multidecadal variability on the global monsoon. *Geophys. Res. Lett.*, **46**, 1765–1775, <https://doi.org/10.1029/2018GL080903>.
- , E. Sanchez-Gomez, M. Gaetani, E. Mohino, and B. Dong, 2020a: Future evolution of the Sahel precipitation zonal contrast in CESM1. *Climate Dyn.*, **55**, 2801–2821, <https://doi.org/10.1007/s00382-020-05417-w>.
- , C. M. Wainwright, M. Sidibe, and A. A. Akinsanola, 2020b: Model uncertainties in climate change impacts on Sahel precipitation in ensembles of CMIP5 and CMIP6 simulations. *Climate Dyn.*, **55**, 1385–1401, <https://doi.org/10.1007/s00382-020-05332-0>.
- Moon, S., and K.-J. Ha, 2020: Future changes in monsoon duration and precipitation using CMIP6. *npj Climate Atmos. Sci.*, **3**, 45, <https://doi.org/10.1038/s41612-020-00151-w>.
- Neelin, J. D., and I. M. Held, 1987: Modeling tropical convergence based on the moist static energy budget. *Mon. Wea. Rev.*, **115**, 3–12, [https://doi.org/10.1175/1520-0493\(1987\)115<0003:MTCBOT>2.0.CO;2](https://doi.org/10.1175/1520-0493(1987)115<0003:MTCBOT>2.0.CO;2).
- Nicholson, S. E., 2013: The West African Sahel: A review of recent studies on the rainfall regime and its interannual variability. *Meteorology*, **2013**, 453521, <https://doi.org/10.1155/2013/453521>.
- Park, J.-Y., J. Bader, and D. Matei, 2015: Northern-Hemispheric differential warming is the key to understanding the discrepancies in the projected Sahel rainfall. *Nat. Commun.*, **6**, 5985, <https://doi.org/10.1038/ncomms6985>.
- , —, and —, 2016: Anthropogenic Mediterranean warming essential driver for present and future Sahel rainfall. *Nat. Climate Change*, **6**, 941–945, <https://doi.org/10.1038/nclimate3065>.
- Pathak, R., S. Sahany, S. K. Mishra, and S. K. Dash, 2019: Precipitation biases in CMIP5 models over the South Asian region. *Sci. Rep.*, **9**, 9589, <https://doi.org/10.1038/s41598-019-45907-4>.
- Persad, G. G., and K. Caldeira, 2018: Divergent global-scale temperature effects from identical aerosols emitted in different regions. *Nat. Commun.*, **9**, 3289, <https://doi.org/10.1038/s41467-018-05838-6>.
- Polson, D., M. Bollasina, G. C. Hegerl, and L. J. Wilcox, 2014: Decreased monsoon precipitation in the Northern Hemisphere due to anthropogenic aerosols. *Geophys. Res. Lett.*, **41**, 6023–6029, <https://doi.org/10.1002/2014GL060811>.
- Randall, D. A., and Coauthors, 2007: Climate models and their evaluation. *Climate Change 2007: The Physical Science Basis*, S. Solomon et al., Eds., Cambridge University Press, 589–662.
- Rowell, D. P., 2003: The impact of Mediterranean SSTs on the Sahelian rainfall season. *J. Climate*, **16**, 849–862, [https://doi.org/10.1175/1520-0442\(2003\)016<0849:TIOMSO>2.0.CO;2](https://doi.org/10.1175/1520-0442(2003)016<0849:TIOMSO>2.0.CO;2).
- , and R. Chadwick, 2018: Causes of the uncertainty in projections of tropical terrestrial rainfall change: East Africa. *J. Climate*, **31**, 5977–5995, <https://doi.org/10.1175/JCLI-D-17-0830.1>.
- Saha, A., and S. Ghosh, 2019: Can the weakening of Indian monsoon be attributed to anthropogenic aerosols? *Environ. Res. Commun.*, **1**, 061006, <https://doi.org/10.1088/2515-7620/ab2c65>.
- Samset, B. H., M. Sand, C. J. Smith, S. E. Bauer, P. M. Forster, J. S. Fuglestedt, S. Osprey, and C.-F. Schleussner, 2018: Climate impacts from a removal of anthropogenic aerosol emissions. *Geophys. Res. Lett.*, **45**, 1020–1029, <https://doi.org/10.1002/2017GL076079>.
- Sandeep, S., and R. S. Ajayamohan, 2015: Poleward shift in Indian summer monsoon low level jetstream under global warming. *Climate Dyn.*, **45**, 337–351, <https://doi.org/10.1007/s00382-014-2261-y>.
- Sanogo, S., A. H. Fink, J. A. Omotosho, A. Ba, R. Redl, and V. Ermert, 2015: Spatio-temporal characteristics of the recent rainfall recovery in West Africa. *Int. J. Climatol.*, **35**, 4589–4605, <https://doi.org/10.1002/joc.4309>.

- Schneider, U., A. Becker, P. Finger, A. Meyer-Christoffer, M. Ziese, and B. Rudolf, 2014: GPCP's new land surface precipitation climatology based on quality-controlled in situ data and its role in quantifying the global water cycle. *Theor. Appl. Climatol.*, **115**, 15–40, <https://doi.org/10.1007/s00704-013-0860-x>.
- Sherman, P., and Coauthors, 2021: Sensitivity of modeled Indian monsoon to Chinese and Indian aerosol emissions. *Atmos. Chem. Phys.*, **21**, 3593–3605, <https://doi.org/10.5194/acp-21-3593-2021>.
- Shi, X., X. Chen, Y. Dai, and G. Hu, 2020: Climate sensitivity and feedbacks of BCC-CSM to idealized CO<sub>2</sub> forcing from CMIP5 to CMIP6. *J. Meteor. Res.*, **34**, 865–878, <https://doi.org/10.1007/s13351-020-9204-9>.
- Shonk, J. K. P., A. G. Turner, A. Chevuturi, L. J. Wilcox, A. J. Dittus, and E. Hawkins, 2020: Uncertainty in aerosol radiative forcing impacts the simulated global monsoon in the 20th century. *Atmos. Chem. Phys.*, **20**, 14 903–14 915, <https://doi.org/10.5194/acp-20-14903-2020>.
- Swart, N. C., and Coauthors, 2019: The Canadian Earth System Model version 5 (CanESM5.0.3). *Geosci. Model Dev.*, **12**, 4823–4873, <https://doi.org/10.5194/gmd-12-4823-2019>.
- Tatebe, H., and Coauthors, 2019: Description and basic evaluation of simulated mean state, internal variability, and climate sensitivity in MIROC6. *Geosci. Model Dev.*, **12**, 2727–2765, <https://doi.org/10.5194/gmd-12-2727-2019>.
- Ueda, H., A. Iwai, K. Kuwako, and M. E. Hori, 2006: Impact of anthropogenic forcing on the Asian summer monsoon as simulated by eight GCMs. *Geophys. Res. Lett.*, **33**, L06703, <https://doi.org/10.1029/2005GL025336>.
- Ullmann, A., B. Fontaine, and P. Roucou, 2014: Euro-Atlantic weather regimes and Mediterranean rainfall patterns: Present-day variability and expected changes under CMIP5 projections. *Int. J. Climatol.*, **34**, 2634–2650, <https://doi.org/10.1002/joc.3864>.
- Urdorf, S., D. Polson, M. A. Bollasina, Y. Ming, A. Schurer, and G. C. Hegerl, 2018: Detectable impact of local and remote anthropogenic aerosols on the 20th century changes of West African and South Asian monsoon precipitation. *J. Geophys. Res. Atmos.*, **123**, 4871–4889, <https://doi.org/10.1029/2017JD027711>.
- van Loon, H., G. A. Meehl, and J. M. Arblaster, 2004: A decadal solar effect in the tropics in July–August. *J. Atmos. Sol.-Terr. Phys.*, **66**, 1767–1778, <https://doi.org/10.1016/j.jastp.2004.06.003>.
- Vecchi, G. A., and B. J. Soden, 2007: Global warming and the weakening of the tropical circulation. *J. Climate*, **20**, 4316–4340, <https://doi.org/10.1175/JCLI4258.1>.
- Voldoire, A., and Coauthors, 2019: Evaluation of CMIP6 DECK experiments with CNRM-CM6-1. *J. Adv. Model. Earth Syst.*, **11**, 2177–2213, <https://doi.org/10.1029/2019MS001683>.
- Wang, B., H.-J. Kim, K. Kikuchi, and A. Kitoh, 2011: Diagnostic metrics for evaluation of annual and diurnal cycles. *Climate Dyn.*, **37**, 941–955, <https://doi.org/10.1007/s00382-010-0877-0>.
- , J. Liu, H.-J. Kim, P. J. Webster, and S.-Y. Yim, 2012: Recent change of the global monsoon precipitation (1979–2008). *Climate Dyn.*, **39**, 1123–1135, <https://doi.org/10.1007/s00382-011-1266-z>.
- , and Coauthors, 2018: Toward predicting changes in the land monsoon rainfall a decade in advance. *J. Climate*, **31**, 2699–2714, <https://doi.org/10.1175/JCLI-D-17-0521.1>.
- , C. Jin, and J. Liu, 2020: Understanding future change of global monsoons projected by CMIP6 models. *J. Climate*, **33**, 6471–6489, <https://doi.org/10.1175/JCLI-D-19-0993.1>.
- Wang, C., D. Kim, A. M. L. Ekman, M. C. Barth, and P. J. Rasch, 2009: Impact of anthropogenic aerosols on Indian summer monsoon. *Geophys. Res. Lett.*, **36**, L21704, <https://doi.org/10.1029/2009GL040114>.
- Wang, H., S.-P. Xie, Y. Kosaka, Q. Liu, and Y. Du, 2019: Dynamics of Asian summer monsoon response to anthropogenic aerosol forcing. *J. Climate*, **32**, 843–858, <https://doi.org/10.1175/JCLI-D-18-0386.1>.
- Wang, P. X., B. Wang, H. Cheng, J. Fasullo, Z. Guo, T. Kiefer, and Z. Liu, 2017: The global monsoon across time scales: Mechanisms and outstanding issues. *Earth-Sci. Rev.*, **174**, 84–121, <https://doi.org/10.1016/j.earscirev.2017.07.006>.
- Wang, Y., J. H. Jiang, and H. Su, 2015: Atmospheric responses to the redistribution of anthropogenic aerosols. *J. Geophys. Res. Atmos.*, **120**, 9625–9641, <https://doi.org/10.1002/2015JD023665>.
- Ward, J. H., 1963: Hierarchical grouping to optimize an objective function. *J. Amer. Stat. Assoc.*, **58**, 236–244, <https://doi.org/10.1080/01621459.1963.10500845>.
- Westervelt, D. M., Y. You, X. Li, M. Ting, D. E. Lee, and Y. Ming, 2020: Relative importance of greenhouse gases, sulfate, organic carbon, and black carbon aerosol for South Asian monsoon rainfall changes. *Geophys. Res. Lett.*, **47**, e2020GL088363, <https://doi.org/10.1029/2020GL088363>.
- Wilcox, L. J., E. J. Highwood, B. B. Booth, and K. S. Carslaw, 2015: Quantifying sources of inter-model diversity in the cloud albedo effect. *Geophys. Res. Lett.*, **42**, 1568–1575, <https://doi.org/10.1002/2015GL063301>.
- , and Coauthors, 2020: Accelerated increases in global and Asian summer monsoon precipitation from future aerosol reductions. *Atmos. Chem. Phys.*, **20**, 11 955–11 977, <https://doi.org/10.5194/acp-20-11955-2020>.
- Willmott, C. J., K. Matsuura, and D. R. Legates, 2001: Terrestrial air temperature and precipitation: Monthly and annual time series (1950–1999), version 1. Center for Climatic Research, [http://climate.geog.udel.edu/~climate/html\\_pages/README\\_ghcn\\_ts2.html](http://climate.geog.udel.edu/~climate/html_pages/README_ghcn_ts2.html).
- Yu, J.-Y., and J. D. Neelin, 1997: Analytic approximations for moist convectively adjusted regions. *J. Atmos. Sci.*, **54**, 1054–1063, [https://doi.org/10.1175/1520-0469\(1997\)054<1054:AAFMC>2.0.CO;2](https://doi.org/10.1175/1520-0469(1997)054<1054:AAFMC>2.0.CO;2).
- Yukimoto, S., and Coauthors, 2019: The Meteorological Research Institute Earth System model version 2.0, MRI-ESM2.0: Description and basic evaluation of the physical component. *J. Meteor. Soc. Japan*, **97**, 931–965, <https://doi.org/10.2151/jmsj.2019-051>.
- Zhang, L., and T. Zhou, 2011: An assessment of monsoon precipitation changes during 1901–2001. *Climate Dyn.*, **37**, 279–296, <https://doi.org/10.1007/s00382-011-0993-5>.
- Zhang, Z., X. Sun, and X.-Q. Yang, 2018: Understanding the interdecadal variability of East Asian summer monsoon precipitation: Joint influence of three oceanic signals. *J. Climate*, **31**, 5485–5506, <https://doi.org/10.1175/JCLI-D-17-0657.1>.
- Zhou, T., W. Zhang, L. Zhang, X. Zhang, Y. Qian, D. Peng, S. Ma, and B. Dong, 2020: The dynamic and thermodynamic processes dominating the reduction of global land monsoon precipitation driven by anthropogenic aerosols emission. *Sci. China Earth Sci.*, **63**, 919–933, <https://doi.org/10.1007/s11430-019-9613-9>.
- Ziehn, T., and Coauthors, 2020: The Australian Earth System Model: ACCESS-ESM1.5. *J. South. Hemisphere Earth Syst. Sci.*, **70**, 193–214, <https://doi.org/10.1071/ES19035>.
- Zuo, M., T. Zhou, and W. Man, 2019: Hydroclimate responses over global monsoon regions following volcanic eruptions at different latitudes. *J. Climate*, **32**, 4367–4385, <https://doi.org/10.1175/JCLI-D-18-0707.1>.